

# Is $\text{Cu}_{3-x}\text{P}$ a Semiconductor, a Metal, or a Semimetal?

Andrea Crovetto,\* Thomas Unold, and Andriy Zakutayev\*



Cite This: *Chem. Mater.* 2023, 35, 1259–1272



Read Online

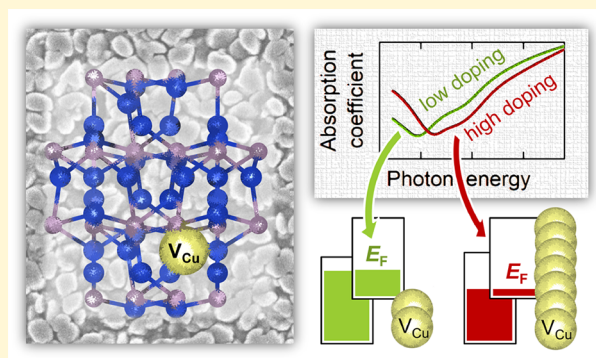
ACCESS |

Metrics & More

Article Recommendations

Supporting Information

**ABSTRACT:** Despite the recent surge in interest in  $\text{Cu}_{3-x}\text{P}$  for catalysis, batteries, and plasmonics, the electronic nature of  $\text{Cu}_{3-x}\text{P}$  remains unclear. Some studies have shown evidence of semiconducting behavior, whereas others have argued that  $\text{Cu}_{3-x}\text{P}$  is a metallic compound. Here, we attempt to resolve this dilemma on the basis of combinatorial thin-film experiments, electronic structure calculations, and semiclassical Boltzmann transport theory. We find strong evidence that stoichiometric, defect-free  $\text{Cu}_3\text{P}$  is an intrinsic semimetal, i.e., a material with a small overlap between the valence and the conduction band. On the other hand, experimentally realizable  $\text{Cu}_{3-x}\text{P}$  films are always p-type semimetals natively doped by copper vacancies regardless of  $x$ . It is not implausible that  $\text{Cu}_{3-x}\text{P}$  samples with very small characteristic sizes (such as small nanoparticles) are semiconductors due to quantum confinement effects that result in the opening of a band gap. We observe high hole mobilities ( $276 \text{ cm}^2/(\text{V s})$ ) in  $\text{Cu}_{3-x}\text{P}$  films at low temperatures, pointing to low ionized impurity scattering rates in spite of a high doping density. We report an optical effect equivalent to the Burstein–Moss shift, and we assign an infrared absorption peak to bulk interband transitions rather than to a surface plasmon resonance. From a materials processing perspective, this study demonstrates the suitability of reactive sputter deposition for detailed high-throughput studies of emerging metal phosphides.



## INTRODUCTION

Most binary compounds consisting of Cu(I) and a moderately electronegative element are interesting semiconductors for optoelectronics and/or thermoelectrics.  $\text{Cu}_2\text{O}$ -based solar cells have reached photovoltaic efficiencies close to 10%.<sup>1</sup>  $\text{Cu}_2\text{O}$  itself is the host of the largest excitonic wave functions ever discovered.<sup>2</sup>  $\text{Cu}_2\text{S}$  was one of the prominent thin-film solar cell materials in the 1970s<sup>3</sup> and later regained prominence in nanoparticle form as a semiconductor system with localized surface plasmon resonances in the near-infrared.<sup>4</sup>  $\text{Cu}_2\text{Se}$  and  $\text{Cu}_2\text{Te}$  are among the best p-type thermoelectric materials known today,<sup>5,6</sup> with record  $zT$  values above 1 at high temperatures.  $\text{CuI}$  is currently the p-type transparent conductor with the highest figure of merit<sup>7,8</sup> and one of the highest-performing transparent thermoelectric materials.<sup>9</sup>  $\text{Cu}_3\text{N}$  is a defect-tolerant semiconductor<sup>10</sup> with an ideal band gap for photovoltaics.<sup>11</sup>  $\text{CuP}_2$  is an unconventional semiconductor containing P–P bonds, with optimal band gap and doping density for photovoltaics.<sup>12</sup>

$\text{Cu}_3\text{P}$  is another copper(I) phosphide, which has been synthesized in the form of single crystals,<sup>13,14</sup> powders,<sup>15–18</sup> thin films,<sup>19–23</sup> and especially nanoparticles and other nanostructured forms.<sup>24–30</sup>  $\text{Cu}_3\text{P}$  is usually found to be strongly p-type due to substantial Cu deficiency<sup>13,17</sup> and is therefore often referred to as  $\text{Cu}_{3-x}\text{P}$ . In recent years,  $\text{Cu}_{3-x}\text{P}$  has been the subject of intense research as an electro- and photocatalyst for various reactions,<sup>20,21,25,27,28,30</sup> as well as a

battery anode.<sup>31,32</sup> However, the current understanding of the electrical and optical properties of  $\text{Cu}_{3-x}\text{P}$  is surprisingly poor. Various authors have identified  $\text{Cu}_{3-x}\text{P}$  as a metal,<sup>14,18,22</sup> many others as a semiconductor,<sup>16,24,26,28–30,33</sup> and in one study it was labeled a semimetal.<sup>27</sup> Device-level applications of  $\text{Cu}_{3-x}\text{P}$  as a semiconducting photovoltaic absorber<sup>24</sup> and as a metallic contact<sup>22</sup> have both been claimed. Furthermore, it is not clear if the electrical properties of  $\text{Cu}_{3-x}\text{P}$  are modified by changing the composition and, in particular, whether  $\text{Cu}_{3-x}\text{P}$  can be doped n-type by nonstoichiometry. The single-phase region of  $\text{Cu}_{3-x}\text{P}$  has only been determined for bulk samples,<sup>13,17,18</sup> with different results obtained in different studies. Finally, the effect of growth temperature and other parameters on the properties of  $\text{Cu}_{3-x}\text{P}$  has not been investigated.

Polycrystalline  $\text{Cu}_{3-x}\text{P}$  thin films are an ideal platform to answer these questions. Unlike the case of nanoparticles, the properties of thin films are not affected by quantum confinement, and electrical and optical properties can be measured more precisely. Compared to single crystals and bulk powders, an advantage of thin films is that their properties can

Received: October 31, 2022

Revised: January 6, 2023

Published: January 25, 2023



rapidly be characterized as a function of elemental composition and process conditions using high-throughput methods.<sup>34–36</sup> Previous thin-film work on  $\text{Cu}_{3-x}\text{P}$  is, however, limited to nonreactive sputter deposition from a  $\text{Cu}_{3-x}\text{P}$  target,<sup>22</sup> chemical vapor deposition,<sup>20</sup> electrodeposition,<sup>19,21</sup> and phosphorization of metallic Cu<sup>23</sup> with only basic materials characterization. A deposition technique amenable to high-throughput experiments is reactive RF sputtering in a  $\text{PH}_3$ -containing atmosphere. Although this technique has rarely been applied to deposit metal phosphides, we have recently shown its feasibility for various phosphide compounds of current interest.<sup>12,37–39</sup>

In this work, we combine high-throughput experiments on reactively sputtered  $\text{Cu}_{3-x}\text{P}$ , first-principles calculations, and semiclassical transport theory. The goal is to investigate the electronic nature of  $\text{Cu}_{3-x}\text{P}$  films as a function of composition and growth conditions. We present strong evidence that  $\text{Cu}_{3-x}\text{P}$  is a p-type semimetal natively doped by Cu vacancies regardless of overall composition and growth conditions. Its single-phase region is likely limited to a narrow range of Cu-deficient compositions. We find that the density of Cu vacancies increases with deposition temperature. We observe an anisotropic electrical conductivity in excellent agreement with the anisotropy of the hole effective masses. Finally, we identify a near-infrared absorption feature somewhat similar to a localized surface plasmon resonance previously reported in  $\text{Cu}_{3-x}\text{P}$  nanoparticles. In thin-film samples, this peak is likely to be an intrinsic feature of bulk  $\text{Cu}_{3-x}\text{P}$  due to interband transitions.

## EXPERIMENTAL AND COMPUTATIONAL DETAILS

$\text{Cu}_{3-x}\text{P}$  thin films were deposited by reactive RF sputtering on borosilicate glass substrates in a  $\text{PH}_3/\text{Ar}$  atmosphere. For experimental throughput purposes, we deposited compositionally graded films by cosputtering a  $\text{Cu}_{3-x}\text{P}$  target and a Cu target facing two opposite sides of the substrate. Each data point and spectrum in the article corresponds to one specific point of these combinatorial films.<sup>34–36</sup>

Elemental composition and film thickness were determined by X-ray fluorescence (XRF). X-ray diffraction (XRD) measurements were conducted using Cu  $K\alpha$  radiation and a 2D detector. Sheet resistance was measured in the substrate plane with a collinear four-point probe. Temperature-dependent Hall carrier concentration and mobility were measured in the substrate plane in the van der Pauw configuration. The complex dielectric function and absorption coefficient were extracted by spectroscopic ellipsometry.

First-principles calculations were performed using density functional theory (DFT) within the projector-augmented wave (PAW) formalism<sup>40</sup> and with a plane-wave basis set as implemented in the GPAW code.<sup>41,42</sup> The Perdew–Burke–Ernzerhof (PBE) exchange correlation functional<sup>43</sup> was employed for structural relaxation. The GLLB-SC exchange correlation functional<sup>44</sup> was employed for electronic ground-state calculations. The complex dielectric function and absorption coefficient were calculated by linear response theory within the Random Phase Approximation (RPA) including local field effects, as implemented in GPAW.<sup>45</sup> Transport properties of  $\text{Cu}_{3-x}\text{P}$  as a function of doping density were estimated using Boltzmann transport theory as implemented in BoltzTraP2.<sup>46</sup> Extensive experimental and computational details are given in the Supporting Information.

## RESULTS

**Growth, Composition, and Structure.** *Growth Routes and Composition.* We initially deposited  $\text{Cu}_{3-x}\text{P}$  films by RF sputtering of a  $\text{Cu}_{3-x}\text{P}$  target in pure Ar, but this process route

does not allow the exploration of a broad parameter space. The films rapidly lose P with increasing deposition temperature (Figure 1a), and Cu/P ratios below 3 are only achievable

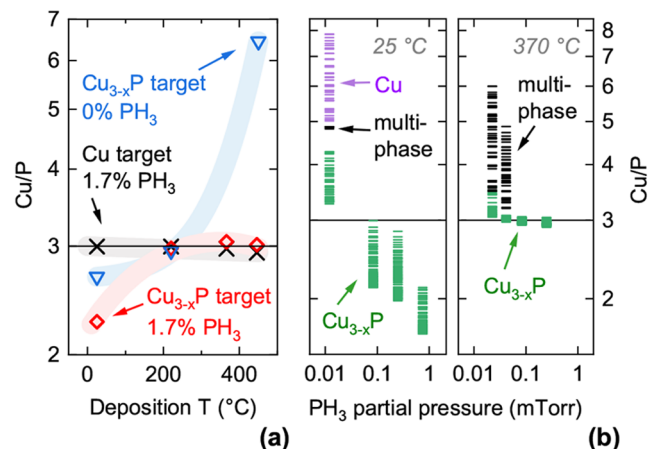


**Figure 1.** Composition and phase analysis of  $\text{Cu}_{3-x}\text{P}$  films under different deposition conditions. (a) Film composition versus deposition temperature. Each data set is indicated by a guiding line. (b) Combinatorial film compositions obtained at different  $\text{PH}_3$  partial pressures by cosputtering a Cu and a  $\text{Cu}_{3-x}\text{P}$  target. Left panel: Room-temperature deposition. Right panel: 370 °C deposition. Data points are colored green, purple, and black when their corresponding XRD patterns contain  $\text{Cu}_{3-x}\text{P}$  peaks only, Cu peaks only, and both types of peaks, respectively.

below  $\sim 250$  °C. Without intentional heating, films are X-ray amorphous (Figure 2). At 220 °C, polycrystalline  $\text{Cu}_{3-x}\text{P}$  grows without detectable secondary phases (Figure 2). At 450 °C, polycrystalline  $\text{Cu}_{3-x}\text{P}$  is still present, but the film has

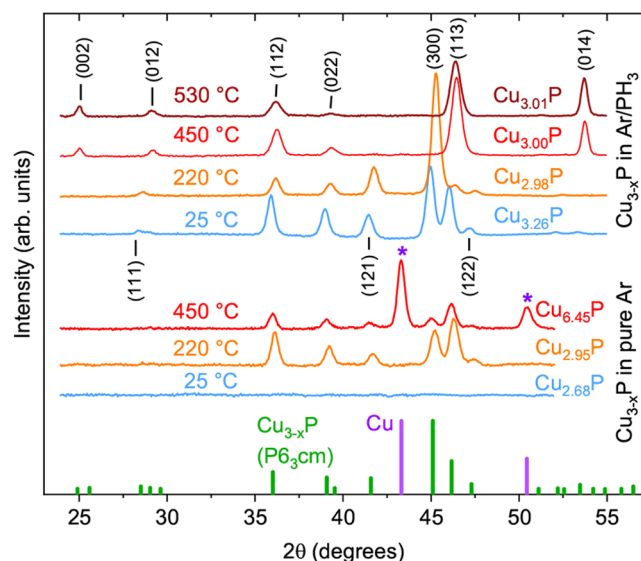


**Figure 2.** Lower data set: XRD patterns of  $\text{Cu}_{3-x}\text{P}$  films deposited in pure Ar from a  $\text{Cu}_{3-x}\text{P}$  target. Upper data set: XRD patterns of  $\text{Cu}_{3-x}\text{P}$  films deposited in a  $\text{PH}_3$ -containing atmosphere by simultaneous sputtering of a  $\text{Cu}_{3-x}\text{P}$  and a Cu target. Film compositions, deposition temperatures, and reference peaks from powder samples<sup>13</sup> are indicated. At room temperature, the inclusion of  $\text{PH}_3$  yields polycrystalline (rather than amorphous) films. Including  $\text{PH}_3$  also prevents P losses at high temperatures.

lost most of its P ( $\text{Cu}/\text{P} \approx 6.5$ ) and mainly consists of large Cu islands (Figure 3). The changes in film morphology with deposition temperature are shown in greater detail in Figure S1.

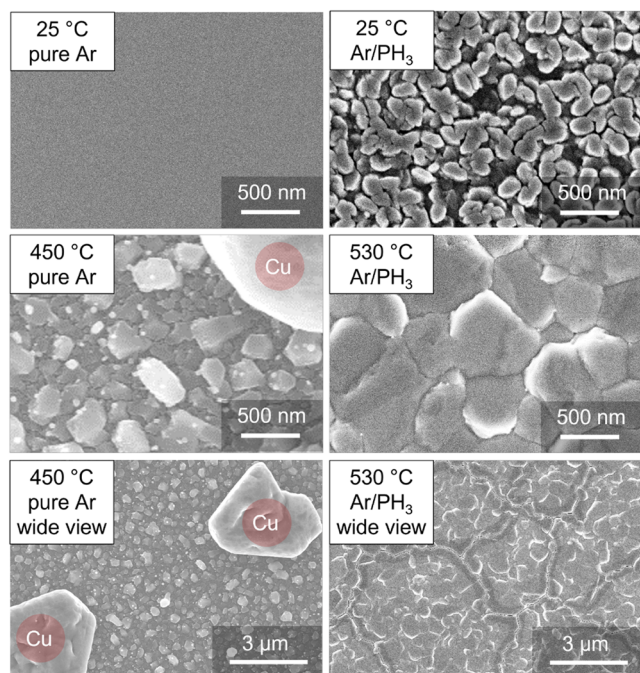


**Figure 3.** SEM images of  $\text{Cu}_{3-x}\text{P}$  films deposited in pure Ar from a  $\text{Cu}_{3-x}\text{P}$  target (left) and in a  $\text{PH}_3$ -containing atmosphere from  $\text{Cu}_{3-x}\text{P}$  and Cu targets (right). A polycrystalline rather than amorphous morphology is found when  $\text{PH}_3$  is included in the growth atmosphere at room temperature (top row). When depositing in pure Ar, most of the phosphorus is already lost at 450 °C, resulting in formation of metallic Cu islands (middle and bottom left). When depositing in Ar/ $\text{PH}_3$ , a homogeneous  $\text{Cu}_{3-x}\text{P}$  film with grains larger than 500 nm can be grown at even higher temperatures (530 °C, middle and bottom right).

Adding  $\text{PH}_3$  to the growth atmosphere significantly expands the conditions under which polycrystalline  $\text{Cu}_{3-x}\text{P}$  can be grown. First, the deposition temperature can be increased up to at least 530 °C (Figures 2 and 3). Second, deposition of  $\text{Cu}_{3-x}\text{P}$  by reactive sputtering of a metallic Cu target becomes possible in the same temperature range as for the  $\text{Cu}_{3-x}\text{P}$  target (Figure 1a). This is a significant process advantage due to the lower cost, higher purity, and higher sputter rate of a metal target. Finally, polycrystalline (rather than amorphous)  $\text{Cu}_{3-x}\text{P}$  is obtained when depositing at room temperature (Figures 2 and 3). This unexpected finding is likely due to a plasma-assisted crystallization process driven by the  $\text{PH}_3$  dissociation products<sup>47</sup> in an RF plasma. In the remainder of the article, we will discuss the properties of  $\text{Cu}_{3-x}\text{P}$  deposited in a  $\text{PH}_3$ -containing atmosphere, unless otherwise specified.

When depositing films at room temperature, a broad range of Cu/P ratios is accessible by tuning the  $\text{PH}_3$  partial pressure (Figure 1b). By simultaneous sputtering of a Cu and a  $\text{Cu}_{3-x}\text{P}$  target facing two opposite sides of the substrate, combinatorial films with a gradient in the Cu/P ratio can be obtained at a single  $\text{PH}_3$  partial pressure (Figure 1b). When depositing at 370 °C, P-rich compositions with Cu/P ratios significantly less than 3 are no longer accessible (Figure 1b). The lowest Cu/P ratios obtained at 370 °C, 450 °C, and 530 °C are 2.89, 2.87,

and 2.91, respectively. Compatibly with our previous study on  $\text{CuP}_2$ ,<sup>12</sup> we assume that other Cu–P phases with Cu/P ratios much less than 3 are unstable at these temperatures, due to the high driving force for P evaporation. All  $\text{Cu}_{3-x}\text{P}$  films were found to be air-stable.

**Phase Analysis.** Regardless of deposition temperature, the XRD patterns of all our  $\text{Cu}_{3-x}\text{P}$  films close to the stoichiometric point are consistent with the  $P6_3cm$  structure<sup>13,18</sup> previously described for bulk samples (see Figure 2). We do not observe any peaks extraneous to the  $P6_3cm$  structure in any of the films with  $\text{Cu}/\text{P} < 3$ , not even in the extremely P-rich films (up to  $\text{Cu}_{1.67}\text{P}$ ) deposited at room temperature. Although polycrystalline secondary phases are absent, we note that  $\text{CuP}_2$  and elemental phosphorus tend to form amorphous phases in bulk samples.<sup>17,48</sup> Even for the case of thin films reactively sputtered at room temperature, we confirmed elsewhere that  $\text{CuP}_2$ <sup>12</sup> and elemental phosphorus<sup>38</sup> are in amorphous form. Thus, amorphous  $\text{CuP}_2$  and/or P secondary phases are very likely to exist when  $\text{Cu}/\text{P} < 2.9$ , which is the most P-rich composition obtainable at temperatures where  $\text{CuP}_2$  and P are no longer stable in the solid state.

In the Cu-rich region ( $\text{Cu}/\text{P} > 3$ ), all films have a composition threshold beyond which XRD peaks from metallic Cu are observed. The range of Cu-rich compositions free of metallic Cu peaks becomes narrower with increasing  $\text{PH}_3$  partial pressure (Figure 1b). As argued in the Supporting Information, this is related to a shift in the prevalent formation mechanism of the  $\text{Cu}_{3-x}\text{P}$  film, from deposition of  $\text{Cu}_{3-x}\text{P}$  vapor to incomplete phosphorization of metallic Cu. In general, XRD results indicate that moderately Cu-rich  $\text{Cu}_{3-x}\text{P}$  films can be grown without precipitation of polycrystalline Cu. However, SEM characterization reveals that some secondary phases are already present at  $\text{Cu}_{3.00}\text{P}$  composition in films deposited above 370 °C (Figure S2). These phases are likely to be noncrystalline Cu. They are no longer visible by SEM at  $\text{Cu}_{2.95}\text{P}$  composition (Figure S2). Thus, the single-phase region of  $\text{Cu}_{3-x}\text{P}$  films deposited at 370 °C and above is probably not wider than the  $\text{Cu}_{2.9}\text{P}$ – $\text{Cu}_{3.0}\text{P}$  range, based on our SEM results. Films deposited at room temperature might have an extended single-phase region on the Cu-rich side, since we could not clearly distinguish secondary phases by SEM in these films. In general, formation of amorphous  $\text{CuP}_2$  (at low temperatures) or P loss (at high temperatures) constrains the single-phase region on the P-rich side. Formation of a Cu secondary phase constrains the single-phase region on the Cu-rich side.

In qualitative agreement with our results, previous studies of bulk  $\text{Cu}_{3-x}\text{P}$  found that single-phase samples always had  $\text{Cu}/\text{P} < 3$ ,<sup>13,17,18,49</sup> although different single-phase stability ranges were found in each study. The stability of these P-rich compositions was generally attributed to a high concentration of Cu vacancies ( $V_{\text{Cu}}$ ), responsible for the high p-type conductivity in  $\text{Cu}_{3-x}\text{P}$ . Previous first-principles calculations confirmed that one  $V_{\text{Cu}}$  per 24-atom unit cell should be thermodynamically stable under a wide range of chemical potentials.<sup>26</sup> In the following sections, we will assume that  $V_{\text{Cu}}$  defects generate most of the charge carriers in  $\text{Cu}_{3-x}\text{P}$  films. This assumption will, however, be justified throughout the article based on our own data.

**Structural Properties.** To evaluate structural changes in  $\text{Cu}_{3-x}\text{P}$  as a function of composition and deposition temperature, we analyze the position of the (113) XRD peak (Figure 4a). In general, the (113) peak shifts to higher diffraction

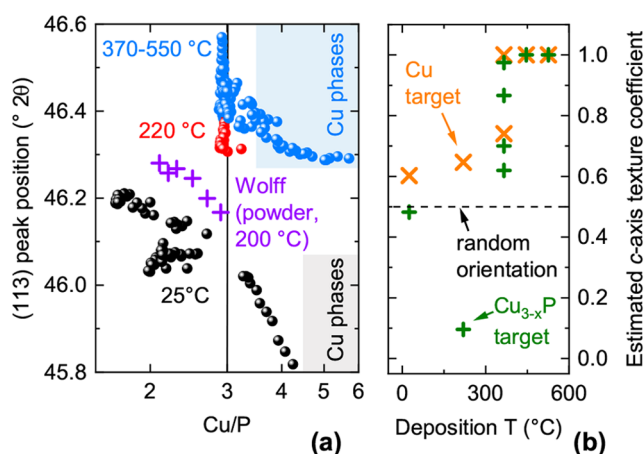


**Figure 4.** Structural parameters of  $\text{Cu}_{3-x}\text{P}$  films. (a) Position of the (113) XRD peak as a function of film composition, grouped by deposition temperature. Analogous data from  $\text{Cu}_{3-x}\text{P}$  powders grown at 200 °C by Wolff et al.<sup>18</sup> are shown. The composition regions where metallic Cu peaks are observed in XRD are shaded in gray (room-temperature deposition) and in blue (370 °C deposition), following the data in Figure 1b. (b) Estimated  $c$ -axis texture coefficient versus deposition temperature, grouped by the target used for deposition. A coefficient of one indicates that the  $c$ -axis is perpendicular to the substrate plane. A coefficient of zero indicates that the  $c$ -axis lies in the substrate plane. The method used to estimate the texture coefficient is described in the Supporting Information.

angles (shorter interplanar distances) with increasing deposition temperature and with decreasing Cu/P ratio. The other peaks in the XRD patterns tend to shift in the same direction (see Figure 2 for some examples). The relative magnitude of the shifts in each XRD pattern is generally compatible with a multiplication of the three lattice constants by a common factor. Hence, we conclude that the (113) peak shifts are indicative of lattice contraction or expansion in all three dimensions. Our data confirm and extend the results by Wolff et al.,<sup>18</sup> who reported contraction of the unit cell in all directions in  $\text{Cu}_{3-x}\text{P}$  powders with decreasing Cu/P ratios (Figure 4a).

For films deposited at 370 °C, the (113) peak stops shifting at high Cu/P ratios, roughly corresponding to the region where we observe precipitation of polycrystalline Cu (blue shaded area in Figure 4a). This suggests that all excess Cu precipitates as a secondary phase rather than being incorporated in the  $\text{Cu}_{3-x}\text{P}$  lattice. For films deposited at room temperature, the (113) peak shift is generally more pronounced up to the precipitation threshold for polycrystalline Cu. Hence, low-temperature-grown  $\text{Cu}_{3-x}\text{P}$  may be able to incorporate substantial Cu excess in the form of defects, a phenomenon that may be linked to the lower volatility of P at low temperatures. This would be a qualitative difference with  $\text{Cu}_{3-x}\text{P}$  grown at higher temperatures, where evidence for Cu precipitation already at Cu/P = 3 has been shown in bulk samples<sup>13,17,18,49</sup> and thin-film samples (this work). As will be shown later, changes in lattice constants are generally correlated to changes in the concentration of Cu vacancies in the different films.

The texture coefficient of  $\text{Cu}_{3-x}\text{P}$  films is shown in Figure 4b as a function of deposition temperature. The  $c$ -axis of the  $\text{Cu}_{3-x}\text{P}$  crystallites has an increasing tendency to align perpendicular to the substrate plane with increasing temperature. Similar  $c$ -axis texturing effects are often observed in other

uniaxially anisotropic materials.<sup>50–52</sup> We also observe that films grown from the Cu target are generally more  $c$ -axis textured than films grown from the  $\text{Cu}_{3-x}\text{P}$  target at the same temperature (Figure 4b and Figure S3).

Finally, Raman spectra of  $\text{Cu}_{3-x}\text{P}$  films do not exhibit any peaks (Figure S4), even though various Raman-active modes are expected for space group  $P6_3cm$ .<sup>53</sup> Raman peaks compatible with a few previous studies<sup>32,33</sup> can only be observed at very high laser excitation intensities above the ablation threshold of  $\text{Cu}_{3-x}\text{P}$ , raising questions on the validity of these previously reported spectra.

**Electrical Properties. Composition Dependence.** The resistivity of the Cu–P system can be mapped over a broad region, from  $\text{Cu}_{1.7}\text{P}$  to  $\text{Cu}_{8.0}\text{P}$ , in films deposited at room temperature (Figure 5a). A local resistivity minimum

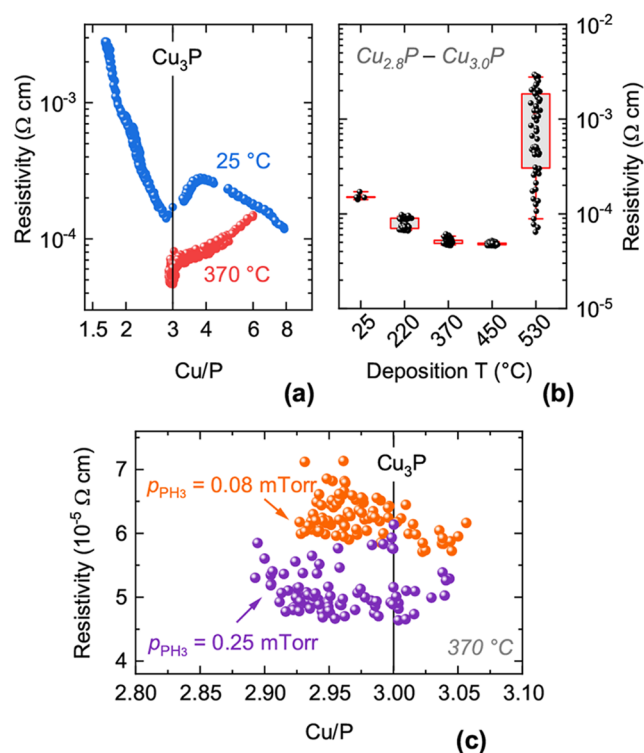


**Figure 5.** Resistivity of  $\text{Cu}_{3-x}\text{P}$  films. (a) Resistivity versus composition for two different deposition temperatures. (b) Resistivity versus deposition temperature (with boxplots) for films in the  $2.8 < \text{Cu}/\text{P} < 3.0$  composition range. (c) Resistivity near the  $\text{Cu}_3\text{P}$  stoichiometric point as a function of  $\text{PH}_3$  partial pressure at 370 °C deposition temperature. The data comes from two combinatorial depositions with different  $\text{PH}_3$  partial pressures. Other material properties (composition ranges, thicknesses, texture coefficients) are very similar in the two data sets.

( $1.4 \times 10^{-4} \Omega \text{ cm}$ ) exists at  $\text{Cu}/\text{P} \approx 2.83$ . The position of the minimum is close to the most P-rich composition that could be obtained at temperatures above 370 °C ( $\text{Cu}_{2.87}\text{P}$ ). This result indicates that further electrical doping by nonstoichiometry is not possible for Cu/P ratios lower than this threshold. Thus, P excess is accommodated by secondary phases rather than defects, in line with the arguments in the previous section. The steep increase in resistivity on the left side of the minimum is due to the much higher resistivity of  $\text{CuP}_2$  (around  $1 \Omega \text{ cm}$ ) with respect to  $\text{Cu}_{3-x}\text{P}$ , as shown elsewhere.<sup>12</sup>

On the right side of the minimum, the resistivity increases until the  $\text{Cu}_{3.8}\text{P}$  composition is reached (Figure 5a). Since metallic Cu peaks begin to appear in XRD at a similar composition (Figure 1b), we assume that the resistivity increase is caused by changes in concentration of point defects up to the Cu precipitation threshold. These defects are also likely to be the cause of unit cell expansion up to a composition of roughly  $\text{Cu}_{4.5}\text{P}$  (Figure 4a). Beyond this threshold, a parallel transport channel along highly conductive Cu percolation paths causes the resistivity to decrease again.

The composition dependence of the resistivity in films deposited at 370 °C (Figure 5a) has some qualitative differences. The minimum resistivity is still found in the vicinity of the stoichiometric point ( $4.6 \times 10^{-5} \Omega \text{ cm}$ ). This value is very similar to the resistivity measured in  $\text{Cu}_{3-x}\text{P}$  single crystals ( $5 \times 10^{-5} \Omega \text{ cm}$ )<sup>14</sup> and a factor of 2 lower than in sintered powders (about  $1.0 \times 10^{-4} \Omega \text{ cm}$ ).<sup>15,18</sup> Hall measurements on a  $\text{Cu}_{2.95}\text{P}$  film indicate p-type conductivity with hole concentration of  $3.81 \times 10^{21} \text{ cm}^{-3}$  and hole mobility of  $28.8 \text{ cm}^2/(\text{V s})$  at room temperature (Figure 6). P-type conductivity is confirmed by measurement of a Seebeck coefficient of  $+11.2 \mu\text{V/K}$  in an analogously deposited film (Figure S5).

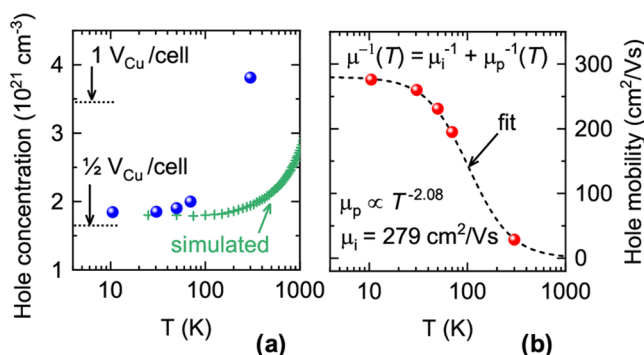


**Figure 6.** Temperature-dependent Hall carrier concentration (a) and Hall mobility (b) of a  $\text{Cu}_{2.95}\text{P}$  film deposited at 370 °C. The hole concentration expected from half and one uncompensated Cu vacancy per 24-atom unit cell (single acceptor) is indicated in (a). Also shown in (a) is the simulated temperature dependence of the Hall hole concentration, as calculated by Boltzmann transport theory on  $\text{Cu}_3\text{P}$  with a Fermi level 0.3 eV below its intrinsic value. The temperature-dependent mobility in (b) is fitted considering two parallel scattering channels (ionized impurities and optical phonons) resulting in the fitting equation shown in the upper part of (b). The best-fit parameters are shown in the lower part of (b).

The  $\text{Cu/P} < 2.9$  region is not experimentally available at a 370 °C deposition temperature, as explained in the previous section. When  $\text{Cu/P} > 3.0$ , the resistivity continues to increase up to the boundary of the investigated composition range ( $\text{Cu/P} \approx 6$ ), despite the fact that Cu secondary phases are already observed at much lower  $\text{Cu/P}$  ratios (Figure 1b). This indicates that transport along  $\text{Cu}_3\text{P}$  channels is a lower-resistance path in these films, even under a substantial presence of Cu secondary phases.

Interestingly, the resistivity in the  $3.2 < \text{Cu/P} < 3.6$  range follows the same trend in two distinct sets of samples: One in which metallic Cu peaks are present in XRD, and another in which they are absent (Figure S2). This finding suggests that a certain amount of Cu secondary phases exist even when they are not detected by XRD, confirming the SEM observations in

Figure S2. Thus, formation of metallic Cu appears to be favored over formation of compensating donors in Cu-rich films. The moderate increase in (113) interplanar spacing for  $\text{Cu/P} > 3$  (Figure 4a) may simply be due to a decrease in  $V_{\text{Cu}}$  concentration. As a consequence, the p-type doping effect of Cu vacancies is never fully compensated by native donors, and  $\text{Cu}_{3-x}\text{P}$  films are always p-type, even when  $\text{Cu/P} > 3.0$ . Accordingly, we did not measure any negative Seebeck coefficients in any film in the  $2.9 < \text{Cu/P} < 3.6$  range.

The average resistivity of films in the vicinity of the stoichiometric point ( $2.8 < \text{Cu/P} < 3.0$ ) decreases with increasing deposition temperature up to 450 °C (Figure 5b). At a higher temperature (530 °C), a higher average resistivity and a much higher standard deviation are observed. This phenomenon is probably linked to an extrinsic effect, i.e., the microscopic cracks visible in SEM images (Figure 3), which are likely detrimental for electrical transport. Analysis of the optical properties (shown later) indicates that the general decrease in resistivity with increasing temperature is likely due to an increase in hole concentration rather than in hole mobility.

A detailed view of the composition-dependent resistivity data close to the stoichiometric point (Figure 5c) reveals that the resistivity depends on the  $\text{PH}_3$  partial pressure during deposition but not on film composition. The overall decrease in resistivity with increasing  $\text{PH}_3$  partial pressure (20% lower resistivity with 3 times higher partial pressure) is expected, since a higher P chemical potential relative to the Cu chemical potential leads to a lower formation energy for Cu vacancies.<sup>26</sup> The complete lack of correlation between resistivity and film composition is more difficult to rationalize, since a higher concentration of Cu vacancies (and thus a lower resistivity) should result in more P-rich compositions. Possible explanations are provided in the Discussion section.

**Temperature Dependence.** Hall effect measurements show that the hole concentration of a low-resistivity  $\text{Cu}_{3-x}\text{P}$  film decreases by a factor 2 from 300 K to 10 K (Figure 6a), in quantitative agreement with previous measurements on powder samples.<sup>18</sup> On the other hand, the hole mobility increases with decreasing temperature up to  $276 \text{ cm}^2/(\text{V s})$  at 10 K, indicating that phonon scattering is the main mobility-limiting mechanism above a few tens of kelvin. At lower temperatures, we expect ionized impurity scattering to be responsible for flattening of the mobility, due to the high density of acceptor defects in  $\text{Cu}_{3-x}\text{P}$ .

We fit the experimental hole mobility  $\mu(T)$  with the expression  $\mu^{-1}(T) = \mu_i^{-1} + \mu_p^{-1}(T)$ . Here,  $\mu_i$  is the mobility resulting from the ionized impurity scattering channel and  $\mu_p(T)$  is the mobility resulting from the phonon scattering channel. We assume that ionized impurity scattering is roughly temperature-independent in a highly doped material like  $\text{Cu}_{3-x}\text{P}$ <sup>39,54</sup> and that phonon-limited mobility can be described by a power law.<sup>55</sup> The fit yields  $\mu_i = 279 \text{ cm}^2/(\text{V s})$  and  $\mu_p = aT^{-2.08}$ , where  $a$  is a temperature-independent factor (Figure 6b). The low-temperature mobility of this  $\text{Cu}_{3-x}\text{P}$  film is remarkably high for a nonepitaxial polycrystalline thin-film material with such a high carrier concentration. An explicit comparison with other materials is provided in the Supporting Information. The mobility of the present  $\text{Cu}_{3-x}\text{P}$  film is also much higher than the mobility of sintered  $\text{Cu}_{3-x}\text{P}$  powders presented in a previous study ( $7.4 \text{ cm}^2/(\text{V s})$  at 300 K and  $38 \text{ cm}^2/(\text{V s})$  at 2 K).<sup>18</sup> Thus, we conclude that  $\text{Cu}_{3-x}\text{P}$  films have very low ionized impurity scattering rates, despite the high density of such impurities ( $V_{\text{Cu}}$  acceptors). The ionized

impurity scattering rate in a highly doped material is expected to scale with  $(m^*/\epsilon_s)^2$ , where  $m^*$  is the carrier effective mass and  $\epsilon_s$  is the static dielectric constant.<sup>56</sup> Since the calculated  $m^*$  for holes in  $\text{Cu}_{3-x}\text{P}$  at the observed carrier concentration is not unusually low (see Discussion section), it is likely that  $\text{Cu}_3\text{P}$  has a high static dielectric constant. In fact, high values of  $\epsilon_s$  are often encountered in narrow band gap semiconductors and semimetals.<sup>57</sup> We emphasize that the electrical properties extracted from Hall measurements are derived under the assumption of a single carrier type, i.e., with holes being much more abundant than electrons. The next sections show that this assumption is probably justified for  $\text{Cu}_{3-x}\text{P}$ .

**Metal, Semimetal, or Degenerately Doped Semiconductor?** The electrical properties of the present  $\text{Cu}_{3-x}\text{P}$  films could be compatible with a metal or a degenerately doped semiconductor. However, previous studies do not agree on to which of the two classes  $\text{Cu}_{3-x}\text{P}$  belongs. Some authors identified it as a metal,<sup>14,18,22</sup> others as a semiconductor.<sup>16,24,26,28–30,33</sup>

Density functional theory (DFT) calculations with the PBE exchange correlation functional<sup>43</sup> yield metallic band structures, both for stoichiometric  $\text{Cu}_3\text{P}$ <sup>58</sup> and for  $\text{Cu}_{3-x}\text{P}$  with 1  $V_{\text{Cu}}$ /unit cell.<sup>26</sup> This is not conclusive evidence that  $\text{Cu}_{3-x}\text{P}$  is a metal, because semiconducting compounds are often incorrectly predicted to be metals at the PBE level due to the well-known “band gap problem” of semilocal functionals.<sup>59</sup> However, stoichiometric  $\text{Cu}_3\text{P}$  is also predicted to be a metal using the hybrid HSE06 functional,<sup>60</sup> with which band gaps are not systematically underestimated.<sup>61</sup> This substantiates the hypothesis that  $\text{Cu}_{3-x}\text{P}$  is intrinsically a metal rather than a degenerately doped semiconductor.

The total density of states (DOS) calculated for stoichiometric  $\text{Cu}_3\text{P}$  at the PBE level (Materials Project ID: mp-7463)<sup>58</sup> is shown in Figure 7a. The DOS calculated at the HSE level is similar.<sup>60</sup> The DOS at the Fermi level is low, with a minimum in its immediate vicinity. Metallic materials with these features (such as graphite, As, and Bi) are often referred to as semimetals, to indicate that there is a small overlap between hole-like bands and electron-like bands at the Fermi level. The limited availability of states at the Fermi level results in smaller charge carrier concentrations than in conventional metals.<sup>62</sup> In addition, semimetals may shift between n-type and p-type behavior with temperature or under relatively small changes in the Fermi level driven by perturbations such as doping, strain, or biasing.<sup>63</sup>

**Semiclassical Simulation of Transport Properties.** It is desirable to check if the experimentally determined properties of  $\text{Cu}_{3-x}\text{P}$  films are compatible with a semimetal. For a direct comparison, we simulated transport properties of  $\text{Cu}_3\text{P}$  at 300 K from the calculated band structure of  $\text{Cu}_3\text{P}$  at the PBE level (Materials Project ID: mp-7463).<sup>58</sup> Net carrier concentrations were derived from the DFT-computed density of states (Figure 7a) and the Fermi distribution function. Other transport quantities (electrical conductivity, conductivity effective masses, Hall carrier concentration, Seebeck coefficient) were calculated by semiclassical Boltzmann transport theory based on an interpolation of the DFT-calculated band structure.<sup>46,64</sup> Two important approximations of the present implementation of Boltzmann transport theory are (i) the carrier scattering time is constant across all bands and energies (we chose 10 fs for reasons explained in the Supporting Information); (ii) doping affects the Fermi level position, but not the band

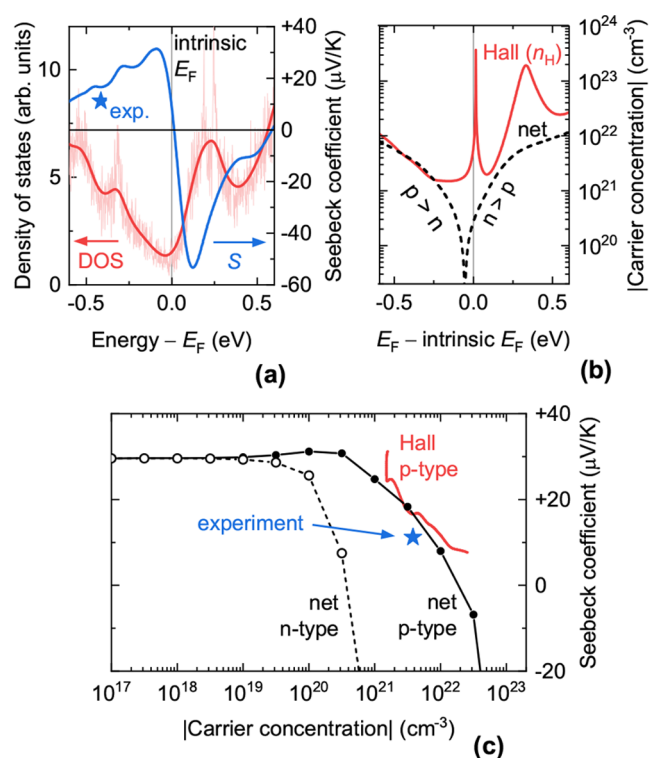


**Figure 7.** Simulated electronic and transport properties of  $\text{Cu}_3\text{P}$  at various doping levels. (a) Total electronic DOS of pristine  $\text{Cu}_3\text{P}$  by DFT (PBE level), extracted from the Materials Project database.<sup>58</sup> The calculated DOS with and without thermal broadening is shown. The low—but not zero—DOS at the Fermi level indicates semimetallicity. Also shown is the simulated Seebeck coefficient as a function of Fermi level position with respect to the intrinsic Fermi level of pristine  $\text{Cu}_3\text{P}$  (zero of the energy scale). The experimental Seebeck coefficient of a  $\text{Cu}_{3-x}\text{P}$  film (star marker) is shown for comparison. (b) Simulated absolute value of the net carrier concentration  $p - n$  and of the Hall carrier concentration  $n_H$  as a function of Fermi level position with respect to the intrinsic Fermi level of pristine  $\text{Cu}_3\text{P}$  (zero of the energy scale). (c) Simulated Pisarenko plots based on the data in (a) and (b). The black data are plotted with the net carrier concentration as the abscissa (p-type for solid data points, n-type for hollow data points). The red data are plotted with the Hall carrier concentration as the abscissa. The star marker indicates the experimental Seebeck coefficient versus experimental Hall hole concentration.

structure itself. The net carrier concentration is defined as  $|p - n|$ , where  $p$  is the free hole concentration and  $n$  is the free electron concentration (both are positive quantities). These carriers can be either intrinsic to the material due to a nonzero DOS at the Fermi level or can be generated by doping.

The Fermi level of intrinsic, defect-free  $\text{Cu}_3\text{P}$  is predicted to lie very close to the DOS minimum (Figure 7a). This intrinsic Fermi level is indicated as the zero of the energy scale in Figure 7a,b. The net carrier concentration in this hypothetical  $\text{Cu}_3\text{P}$  without any dopants is  $3 \times 10^{20} \text{ cm}^{-3}$  (about one net electron per 250 atoms; see dashed line in Figure 7b). This intrinsic electron concentration arises from the nonzero DOS (and, thus, nonzero free electron density) of  $\text{Cu}_3\text{P}$  at the Fermi level. As the Fermi level shifts down through p-type doping, the net carrier concentration vanishes around 60 meV below the intrinsic Fermi level. At this energy, the intrinsic electrons are fully compensated by holes generated by doping. Upon further p-type doping, holes dominate the conductivity rather than

electrons. This net carrier concentration is not directly measured by the Hall effect. Instead, the Hall carrier concentration (positive or negative) is defined as  $n_H = 1/eR_H$ , where  $R_H$  is the Hall coefficient and  $e$  is the elementary charge. When both electrons and holes contribute to the conductivity

$$R_H = \frac{p\mu_h^2 - n\mu_e^2}{e(p\mu_h + n\mu_e)^2} \quad (1)$$

where  $\mu_h$  and  $\mu_e$  are the (positive) mobilities of holes and electrons, respectively.<sup>65</sup> In the transport calculations, the mobilities are obtained from the conductivity effective masses  $m_{e,h}^*$ <sup>46,64</sup> and the assumed scattering time  $\tau$  as  $\mu_{h,e} = e\tau/m_{e,h}^*$ . From eq 1, it is apparent that the Hall concentration deviates from the simple net carrier concentration ( $p - n$ ), unless electrons and holes have very different concentrations. This discrepancy is highlighted by calculating ( $p - n$ ) and  $n_H$  in  $\text{Cu}_3\text{P}$  as a function of the Fermi level (Figure 7b). The discrepancy between ( $p - n$ ) and  $n_H$  is particularly evident in materials predicted to be semimetallic (like  $\text{Cu}_3\text{P}$ ) because of the comparable concentrations of electrons and holes. Some counterintuitive features arise from this effect: (1) the Hall carrier concentration is predicted to always be above  $1.5 \times 10^{21} \text{ cm}^{-3}$  even when the net carrier concentration is very low; (2) the Hall carrier concentration is expected to diverge about 10 meV above the intrinsic Fermi level; and (3) there is a small Fermi level range where the simulations predict that  $\text{Cu}_3\text{P}$  will appear as p-type from a Hall measurement, even though electrons are more abundant than holes. These points are further discussed in the Supporting Information.

The calculated Seebeck coefficient  $S$  changes sign at roughly the same Fermi level as  $R_H$  (Figure 7a). When both electrons and holes contribute to the conductivity,

$$S = \frac{p\mu_h S_h + n\mu_e S_e}{p\mu_h + n\mu_e} \quad (2)$$

where  $S_h$  (positive) and  $S_e$  (negative) are the Seebeck coefficients for holes and electrons alone, respectively.<sup>65</sup> As expected, lowering and raising the Fermi level in the simulation leads to positive and negative Seebeck coefficients, respectively. In summary, a Hall effect measurement and a thermovoltage measurement on a  $\text{Cu}_{3-x}\text{P}$  sample are expected to yield the same conductivity type.

**Comparison with Experiment.** The experimentally measured Hall carrier concentration at 300 K ( $3.81 \times 10^{21} \text{ cm}^{-3}$ ) corresponds to a Fermi level 0.41 eV below the intrinsic Fermi level according to Figure 7b. The experimental and calculated Seebeck coefficients at this Fermi level (+11.2  $\mu\text{V}/\text{K}$  and +16.6  $\mu\text{V}/\text{K}$ , respectively) are in reasonable agreement. This is also visualized in the Pisarenko plot (Seebeck coefficient versus carrier concentration) in Figure 7c.

Our experimental results are consistent with a p-type semimetal doped with approximately one Cu vacancy per 24-atom unit cell, for two reasons. First, we expect the Fermi level of  $\text{Cu}_{3-x}\text{P}$  with 1  $V_{\text{Cu}}$ /unit cell to lie about 0.3 eV lower than the Fermi level of a pristine  $\text{Cu}_3\text{P}$  semimetal. This Fermi level position is estimated by aligning the localized Cu 3d states of the respective band structures,<sup>26</sup> following a standard methodology used in band alignment measurements by photoemission spectroscopy.<sup>66</sup> The magnitude of the Fermi level shift is experimentally confirmed by quantifying the blue shift of the

absorption coefficient spectrum of doped  $\text{Cu}_{3-x}\text{P}$  versus pristine  $\text{Cu}_3\text{P}$  (Figure 8e, discussed later).

Second, the hole concentration corresponding to one ionized Cu vacancy per unit cell ( $3.3 \times 10^{21} \text{ cm}^{-3}$ ) minus the intrinsic free electrons concentration ( $3 \times 10^{20} \text{ cm}^{-3}$ ) is 3.0

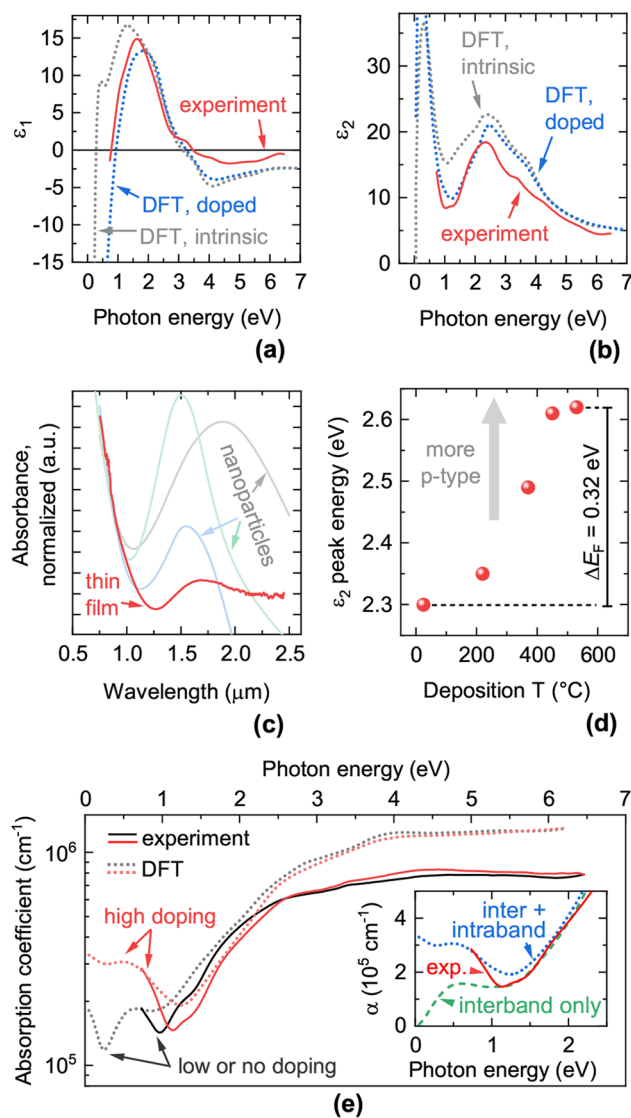


**Figure 8.** Optical properties of  $\text{Cu}_{3-x}\text{P}$  films. (a, b) Real ( $\epsilon_1$ ) and imaginary part ( $\epsilon_2$ ) of the dielectric function. Experimental spectra were measured by ellipsometry. Simulated spectra were calculated by DFT on intrinsic  $\text{Cu}_3\text{P}$  and on doped  $\text{Cu}_{2.83}\text{P}$  with 1  $V_{\text{Cu}}$ /unit cell. (c) NIR absorbance derived from transmission and reflection measurements. Previously reported absorbances of  $\text{Cu}_{3-x}\text{P}$  nanoparticles<sup>24,26,29</sup> are also shown. (d) Photon energy of the peak found in experimental  $\epsilon_2$  spectra (see Figure S6) as a function of deposition temperature. The shift in peak energy is attributed to a Burstein–Moss shift. (e) Absorption coefficient  $\alpha$ . The experimental  $\alpha$  from a high-resistivity  $\text{Cu}_{3-x}\text{P}$  film is compared to the DFT-calculated  $\alpha$  for intrinsic  $\text{Cu}_3\text{P}$  (“low or no doping” label). The experimental  $\alpha$  from a low-resistivity  $\text{Cu}_{3-x}\text{P}$  film is compared to the DFT-calculated  $\alpha$  for doped  $\text{Cu}_{2.83}\text{P}$  (“high doping” label). (e, inset) Comparison of experimental and calculated  $\alpha$  spectra in the IR. One calculated spectrum (dashed line) only includes interband transitions. The other calculated spectrum (dotted line) includes both intraband and interband transitions.

$\times 10^{21} \text{ cm}^{-3}$ . This value is close to the experimentally determined Hall carrier concentration of  $3.8 \times 10^{21} \text{ cm}^{-3}$  at 300 K (Figure 6a). At these p-type doping levels,  $p \gg n$  and the Hall carrier concentration closely follows the net carrier concentration (Figure 7b). Hence, interpreting Hall effect data assuming a single carrier type is justified, and the Hall mobility (Figure 6b) should reflect the mobility of the holes. The experimentally observed decrease in Hall hole concentration with decreasing temperature is confirmed by Boltzmann transport theory, although not quantitatively. A more detailed discussion is given in the Supporting Information. To conclude, the electrical properties of  $\text{Cu}_{3-x}\text{P}$  films are generally compatible with a semimetallic band structure.

**Optical Properties. Optical Signatures of Semimetallicity.** The optical properties of  $\text{Cu}_{3-x}\text{P}$  films provide additional evidence that  $\text{Cu}_{3-x}\text{P}$  is a semimetal rather than a semiconductor. The real and imaginary parts of the dielectric function ( $\epsilon_1$  and  $\epsilon_2$ , respectively) were measured by ellipsometry on low-resistivity films (Figure 8a,b). When the photon energy decreases from the visible to the infrared (IR),  $\epsilon_1$  becomes negative and  $\epsilon_2$  increases, as expected for a material with a high concentration of free carriers.<sup>67</sup>

We also calculated the dielectric function by DFT using linear response theory and the random phase approximation<sup>41</sup> (details in the Supporting Information). The calculation on intrinsic  $\text{Cu}_3\text{P}$  is in reasonably good agreement with the experimental spectra (Figure 8a,b). However, the sign change of  $\epsilon_1$  in the IR occurs at  $\sim 0.5 \text{ eV}$  lower photon energy than in the experimental spectrum. This may be due to the higher carrier concentration in the experimental sample ( $\sim 4 \times 10^{21} \text{ cm}^{-3}$ ) than in the intrinsic  $\text{Cu}_3\text{P}$  system considered in the calculation ( $\sim 3 \times 10^{20} \text{ cm}^{-3}$ ; see previous section). To test this hypothesis, we repeated the dielectric function calculation on structurally relaxed  $\text{Cu}_{2.83}\text{P}$  with one Cu vacancy per unit cell. Indeed, the sign change of  $\epsilon_1$  shifts to higher photon energies, and the agreement with experiment becomes very good over the whole  $0.7 \text{ eV}$ – $6.5 \text{ eV}$  spectral range (Figure 8a,b). Again, we emphasize that the calculated dielectric function was derived from an originally semimetallic band structure under the presence of one Cu vacancy per unit cell. Thus, the agreement between experiment and theory is a further indication that  $\text{Cu}_{3-x}\text{P}$  films are p-type semimetals doped by about one Cu vacancy per unit cell.

**Near-Infrared Response.** To obtain more experimental information on the optical properties of  $\text{Cu}_{3-x}\text{P}$  films in the near-infrared (NIR), we determined their absorbance from transmission and reflection measurements with an extended IR range (Figure 8c). Interestingly, the films exhibit a NIR absorption peak rather than the continuously increasing absorbance with decreasing photon energy characteristic of free carrier absorption. The peak maximum is around  $1.7 \mu\text{m}$  ( $0.73 \text{ eV}$ ). As shown in Figure 8c, the peak position and width are compatible with previous reports of a localized surface plasmon resonance (LSPR) peak in  $\text{Cu}_{3-x}\text{P}$  nanoparticles,<sup>24,26,68</sup> although its intensity relative to the main absorption band in the visible is lower than that of the LSPR peak.

Since our sample is a continuous film rather than disconnected nanoparticles, the NIR peak might be due to a (nonlocalized) surface plasmon polariton (SPP) instead of a LSPR. Surface plasmons cannot be excited by light at perfectly planar surfaces due to the requirement of momentum conservation between the plasmon and the photon.<sup>69</sup>

However, the presence of substantial surface roughness can relax this requirement, so SPPs have been observed, for example, in rough Ag films by simple reflection measurements.<sup>69,70</sup>

A problem with the interpretation of the NIR peak as an SPP is that this peak is observed in all our measured  $\text{Cu}_{3-x}\text{P}$  samples—even in thinner films processed at room temperature, which have very low surface roughness. An alternative interpretation of the NIR peak is offered by plotting DFT-calculated absorption coefficients (Figure 8e), which do not include any plasmonic effects and are only representative of the bulk optical properties of  $\text{Cu}_{3-x}\text{P}$ . Intriguingly, the calculations for both intrinsic  $\text{Cu}_3\text{P}$  and p-type doped  $\text{Cu}_{2.83}\text{P}$  reveal a peak centered at around  $0.6 \text{ eV}$  photon energy. When only interband transitions are included in the calculation on doped  $\text{Cu}_{2.83}\text{P}$  (inset of Figure 8e, green dashed line), the NIR peak is still present but the absorption coefficient approaches zero at zero photon energy. When both interband and intraband transitions are included in the calculation (inset of Figure 8e, blue dotted line), the NIR peak exists on top of an additional background of increasing absorption coefficient with decreasing photon energy. This background is due to free carrier absorption, i.e., the absorption of low-energy photons by carriers near the Fermi level, which are promoted to states close in energy available within the same band. Note that this free carrier absorption background occurs at much lower photon energies in intrinsic  $\text{Cu}_3\text{P}$  (up to  $0.3 \text{ eV}$ ) than in doped  $\text{Cu}_{2.83}\text{P}$  (up to  $1.2 \text{ eV}$ ) as expected from Drude theory.

To sum up, the NIR peak in  $\text{Cu}_{3-x}\text{P}$  is likely due to bulk interband transitions, which are independent of both plasmonic effects and the free carrier density. A simultaneous SPP response in the same spectral range cannot be excluded, but it is difficult to deconvolve, due to overlap with the bulk response. The findings presented in this section can help rationalize why the NIR peak in thin films is much less intense than in nanoparticles and why the absorbance sharply decreases again at longer wavelengths in nanoparticles but not in films (Figure 8c). The first effect occurs because the NIR peak has a different origin in the two cases (bulk interband transitions in the films, LSPR in the nanoparticles). The second effect occurs because intraband transitions in very small nanoparticles are obscured by their intense surface plasmonic response. This does not occur in a thicker film free of quantum confinement effects.

**Burstein–Moss Shift.** Comparing again the measured absorption coefficients of the two  $\text{Cu}_{3-x}\text{P}$  films shown in Figure 8e, we notice that the higher-doping (lower-resistivity) film exhibits an overall blue-shift of the absorption coefficient spectrum at all measured photon energies (Figure 8e). This effect is not related to absorption by free carriers or plasmons. Instead, it has a similar origin as the Burstein–Moss effect observed in degenerately doped semiconductors.<sup>71,72</sup> It is caused by the lowering of the Fermi level with increasing p-type doping. The lower Fermi level causes optical transitions to collectively shift to higher photon energies, because the initial states of the transitions are shifted to deeper energies in the  $\text{Cu}_{3-x}\text{P}$  band structure, so higher-energy transitions are required to reach the same final states. Similar to other optical features of  $\text{Cu}_{3-x}\text{P}$ , the Burstein–Moss shift is also predicted by DFT, as evident by comparing the measured and calculated absorption coefficients in Figure 8e.

We quantified the Burstein–Moss shifts in the lowest-resistivity films at each deposition temperature by finding the

photon energy at which their  $\epsilon_2$  has a maximum (Figure S6). The Burstein–Moss shift become progressively larger as the temperature increases (Figure 8d), indicating that films deposited at higher temperatures are more p-type. This result shows that the electrically probed decrease in resistivity with deposition temperature (Figure 5b) is at least partially due to an increase in hole concentration. It also shows that the increase in resistivity at 530 °C deposition temperature (Figure 5b) is due to a decrease in mobility, probably due to cracks in the films. If it were due to a decrease in hole concentration, the Burstein–Moss shift would not keep increasing at this temperature. The continuously increasing hole concentration with deposition temperature follows the previously predicted increase in Cu vacancy concentration with temperature beyond 1  $V_{\text{Cu}}$ /unit cell using Boltzmann statistics.<sup>26</sup>

Finally, we note that the difference in the Burstein–Moss shifts between the films with the smallest and largest shifts (deposited at room temperature and 530 °C, respectively) is 0.32 eV. This result is compatible with our calculations of carrier concentration versus Fermi level, which predicted a lowering of the Fermi level by 0.415 eV between intrinsic  $\text{Cu}_3\text{P}$  and  $\text{Cu}_{3-x}\text{P}$  with  $n_{\text{H}} = 3.8 \times 10^{21} \text{ cm}^{-3}$  (Figure 7b). It is also compatible with the  $\sim 0.3$  eV Fermi level down-shift extracted from the previously calculated band structure of  $\text{Cu}_{2.83}\text{P}$  with a 1  $V_{\text{Cu}}$ /unit cell.<sup>26</sup> These findings confirm that experimental  $\text{Cu}_{3-x}\text{P}$  samples are semimetals rather than conventional metals, because the much higher DOS at the Fermi level characteristic of a conventional metal would imply a much smaller Fermi level shift upon doping.

## DISCUSSION

**Effect of  $\text{PH}_3$  Plasma on Sputter Deposition of  $\text{Cu}_{3-x}\text{P}$ .** Five important roles of  $\text{PH}_3$  in the sputter deposition of  $\text{Cu}_{3-x}\text{P}$  can be identified. First,  $\text{PH}_3$  is a source of P that enables growth of  $\text{Cu}_{3-x}\text{P}$  from a metallic Cu target. Second, the presence of  $\text{PH}_3$  counteracts the tendency of  $\text{Cu}_{3-x}\text{P}$  to decompose at elevated temperatures, enabling relatively high-temperature deposition where large crystal grains,  $c$ -axis texturing, and a higher  $V_{\text{Cu}}$  concentration can be achieved. Third, a very broad range of Cu/P ratios can be obtained at room temperature (Figure 5a), where P losses are minor. This possibility has allowed us to grow polycrystalline  $\text{CuP}_2$  films by a two-step process.<sup>12</sup> Fourth,  $\text{PH}_3$  assists the crystallization of  $\text{Cu}_{3-x}\text{P}$  even at room temperature, where films sputtered in pure Ar are amorphous (Figure 2). This effect is presumably caused by bombardment of the growing film by energetic species formed from the dissociation of  $\text{PH}_3$  in an RF plasma.<sup>47</sup> Fifth, the net concentration of electrically active defects can be tuned by adjusting the  $\text{PH}_3$  partial pressure, independently of film composition (Figure 5c). This effect is a reminder that equilibrium defect concentrations ultimately depend on chemical potentials during growth, and not directly on film composition. The beneficial features listed in this section demonstrate that reactive RF sputtering is a highly versatile route for both fundamental studies of new phosphides and their technological development.

**Structural–Electrical Property Relationships.** In Figure 4, we identified large variations in lattice constants and preferential orientation in  $\text{Cu}_{3-x}\text{P}$  films processed under different conditions. Here, we investigate possible relationships between these structural trends and the electrical properties of the films. In general, the lattice constants of  $\text{Cu}_{3-x}\text{P}$  films tend to decrease with increasing electrical conductivity. This

behavior is shown in Figure 9a by measuring the (113) plane spacing in combinatorial samples with different

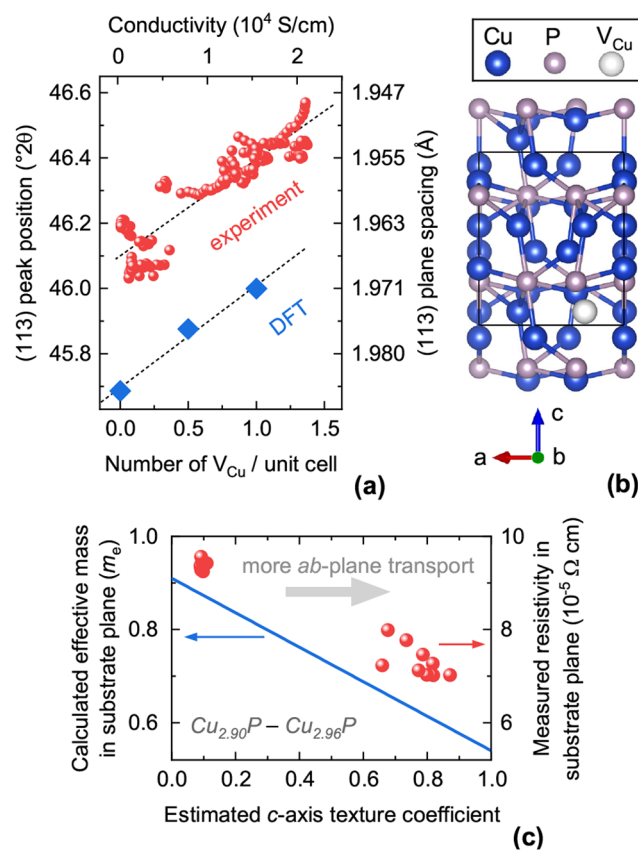


**Figure 9.** Relationships between structural and electrical properties in  $\text{Cu}_{3-x}\text{P}$  films. (a) Spacing between (113) planes (determined from XRD peak position) as a function of measured conductivity. Also shown is the DFT-calculated (113) plane spacing for the case of zero, half, and one Cu vacancy per 24-atom unit cell. The conductivity axis and the  $V_{\text{Cu}}$  concentration axis are linked by assuming a constant mobility of  $29 \text{ cm}^2/(\text{V s})$  (Figure 6b). (b) The  $P6_3cm$  crystal structure of  $\text{Cu}_3\text{P}$ .<sup>73</sup> The unit cell and the energetically preferred site for  $V_{\text{Cu}}$  are shown. (c) Experimentally measured resistivity as a function of the estimated  $c$ -axis texture coefficient. A coefficient of one indicates that the resistivity in the  $ab$ -plane is probed. A coefficient of zero indicates that the resistivity in a  $c$ -axis-containing plane is probed. Only films deposited at 220 °C with  $2.90 < \text{Cu/P} < 2.96$  are considered. The average conductivity effective mass of  $\text{Cu}_{3-x}\text{P}$  in the probed transport plane is also plotted versus the texture coefficient, showing that the changes in resistivity can be explained by changes in the effective mass with lattice direction.

conductivities. As noted earlier in this article, changes in the interplanar spacing in other directions indicate an overall unit cell contraction or expansion in all directions, rather than strain in one particular direction.

A simple explanation for this phenomenon is that the unit cell contracts when Cu vacancies are formed. Unit cell contraction is expected since the atoms surrounding the Cu vacancy can be packed closer together due to the free space left by the missing Cu atom. Very limited charge transfer is expected between Cu and P, due to the semimetallic (rather than ionic) nature of  $\text{Cu}_{3-x}\text{P}$ . Hence, the counteracting effect of anion–anion repulsion, which may lead to unit cell expansion, is likely negligible. To verify this behavior, we

employed DFT to calculate the equilibrium lattice constants of  $\text{Cu}_{3-x}\text{P}$  in the presence of zero, half, and one Cu vacancy per unit cell. The Cu vacancy was placed in one of the symmetry-equivalent Cu(1) lattice sites following Olofsson's notation.<sup>13</sup> This site is indicated in Figure 9b and was previously found to be the most energetically favorable site for  $V_{\text{Cu}}$ .<sup>26</sup> As expected, the structure relaxes to lower lattice constants with increasing  $V_{\text{Cu}}$  concentration. For one vacancy per unit cell, the  $a$ ,  $b$ , and  $c$  axes decrease by 0.56%, 0.65%, and 0.63% with respect to the intrinsic cell, respectively. The resulting (113) plane spacing for the calculated structures is shown in Figure 9a as a function of  $V_{\text{Cu}}$  concentration. The rate of change in the interplanar spacing is in quantitative agreement with the experimental behavior. The overall overestimation of lattice constants is a known problem of the PBE functional used for the relaxation.<sup>74</sup> This result substantiates the hypotheses that (i) changes in  $V_{\text{Cu}}$  concentration are the main source of conductivity changes in  $\text{Cu}_{3-x}\text{P}$  films and (ii) the estimate of 1–1.5  $V_{\text{Cu}}$  per unit cell for the most electrically conductive films is reasonable.

Clearly, the decrease in lattice constants with increasing conductivity is only a rough experimental trend. Other factors such as defect compensation and variations in mobility are likely to affect the conductivity of a given film. For example, we may expect different hole mobilities  $\mu$  in the  $ab$ -plane and along the  $c$ -axis, since the  $P6_3cm$  structure of  $\text{Cu}_{3-x}\text{P}$  is uniaxially anisotropic (Figure 9b). Under a p-type doping density of  $3 \times 10^{21} \text{ cm}^{-3}$  at room temperature, we find a conductivity effective mass of  $0.54 m_e$  in the  $ab$ -plane and of  $1.28 m_e$  along the  $c$ -axis by applying Boltzmann transport theory. Assuming a direction-independent carrier scattering time  $\tau$ , one would expect the resistivity  $\rho$  to be proportional to the effective mass  $m^*$  in the transport direction, due to the  $\rho \propto \mu^{-1} \propto m^* \tau^{-1}$  relationships. To test this hypothesis, we consider the  $\text{Cu}_{3-x}\text{P}$  samples deposited at 220 °C. They were grown in the same deposition run, have similar composition ( $\text{Cu}_{2.90}\text{P}$ – $\text{Cu}_{2.96}\text{P}$ ), but have large differences in orientation with respect to the substrate depending on the prevalence of  $\text{Cu}_{3-x}\text{P}$  formation at the target or at the substrate (Figure S3). Indeed, we find that the resistivity measured in the plane of the substrate is proportional to the average effective mass in the plane of the substrate, derived from the estimated texture coefficient (Figure 9c). Assuming that the changes in resistivity are caused by changes in hole mobility, this correlation provides experimental evidence for enhanced hole mobility in the  $ab$  plane. It is also an indirect indication that the carrier scattering time at room temperature is not strongly direction-dependent.

**Consequences of Nonstoichiometry.** We have seen that the net concentration of acceptor defects increases with deposition temperature (Figures 5b and 8d) and  $\text{PH}_3$  partial pressure (Figure 5c). We have also gathered substantial evidence that these acceptors are Cu vacancies. However, an apparent discrepancy requires further discussion. A large fraction of films are expected to have a  $V_{\text{Cu}}$  concentration between 1 and 1.5 per unit cell (Figures 6a and 9a). These concentrations would correspond to Cu/P ratios between 2.75 and 2.83 in films without secondary phases or compensating defects. Yet, the most P-rich composition obtained in low-resistivity films is  $\text{Cu}_{2.87}\text{P}$ . This compositional discrepancy is only 4% and may well be due to a small systematic error in the evaluation of elemental composition (see the Supporting Information). However, we also find that the electrical

resistivity and the overall composition in the  $2.95 < \text{Cu}/\text{P} < 3.05$  range are completely uncorrelated (Figure 5c). This finding cannot be explained by measurement errors, because we estimate the error of relative composition measurements to be lower than 1% (more details in the Supporting Information).

A possible explanation is the existence of metallic Cu secondary phases for  $\text{Cu}/\text{P} > 2.75$ , so even in highly P-rich films. As discussed in the Supporting Information, this mechanism is incompatible with other experimental observations in this study. The presence of other point defects beyond Cu vacancies could be an alternative explanation for the composition-independent resistivity around the stoichiometric point. As discussed in the Supporting Information, different types of defects could potentially explain the experimental results—either extrinsic impurities or native defects and either donor- or charge-neutral defects. Some defects that would be compatible with our results are  $\text{Cu}_\text{P}$  (either donors or neutrals),  $\text{H}_\text{i}$  donors, or  $\text{H}_{\text{Cu}}$  neutrals. Hydrogen-related defects may result from H incorporation in a reactive film deposition process involving  $\text{PH}_3$  such as ours.<sup>75</sup> A more extensive qualitative discussion of possible defects is given in the Supporting Information.

Besides point defects, there are other mechanisms that may change the overall film composition without changing the net dopant concentration. They are intermediate between formation of isolated point defects and segregation of secondary phases. One mechanism is the formation of Cu-rich donor–acceptor defect clusters such as  $(V_{\text{Cu}} + \text{Cu}_\text{P})$ . Another possible mechanism is extended clustering driven by entropy.<sup>76</sup> A dedicated study of defect energetics in  $\text{Cu}_{3-x}\text{P}$  may help clarify which mechanism is dominant.

**On the Previous Identification of  $\text{Cu}_{3-x}\text{P}$  as a Semiconductor.** As mentioned earlier in this article, many authors have identified  $\text{Cu}_{3-x}\text{P}$  as a degenerately doped semiconductor, rather than a (semi)metal.<sup>16,24,26,28–30,33</sup> In many of these studies, the characterized samples were  $\text{Cu}_{3-x}\text{P}$  nanoparticles or nanoplatelets with a characteristic size of less than 10 nm. In these cases, it is possible that size effects (quantum confinement) result in the opening of a band gap in an otherwise (semi)metallic system. A similar effect is known for 1T-TiS<sub>2</sub>.<sup>77</sup> However, the results of our study also demonstrate that many criteria previously used to assign semiconducting behavior to  $\text{Cu}_{3-x}\text{P}$  are not at all incompatible with a semimetal.

For example, several studies identified  $\text{Cu}_{3-x}\text{P}$  as a semiconductor with a band gap in the 0.8 eV–1.7 eV range.<sup>16,28,30,33</sup> This assignment was justified by the observation of an absorption onset in this photon energy range. However, Figure 8e demonstrates that the photon energy of the absorption onset is not related to a band gap, but it depends instead on the energy at which interband absorption becomes dominant over intraband (free-carrier) absorption. The photon energy of this apparent “band gap” ultimately depends on the free carrier density in the semimetal. If we remove the source of free carrier absorption (intraband transitions), we see that the absorption coefficient of  $\text{Cu}_{3-x}\text{P}$  only approaches zero at zero photon energy, indicating that its band gap is zero (inset of Figure 8e, green dashed line).

In other cases, identification of  $\text{Cu}_{3-x}\text{P}$  as a semiconductor was based on the detection of a positive Seebeck coefficient<sup>26</sup> or of a photovoltaic effect.<sup>24</sup> However, Boltzmann transport theory predicts positive Seebeck coefficients in semimetallic

Cu<sub>3</sub>P, both under intrinsic- and p-type-doped conditions (Figure 7a). Many elemental metals also have positive Seebeck coefficients.<sup>62</sup> A photovoltaic effect was observed in a Cu<sub>3-x</sub>P/CdS heterojunction.<sup>24</sup> However, CdS is itself a photovoltaic material, and the reported photovoltaic parameters are compatible with a CdS-based solar cell in which Cu<sub>3-x</sub>P acts as a contact. In particular, the reported short-current density of 2.7 mA/cm<sup>2</sup> is well within the Shockley–Queisser limit<sup>78</sup> of 7.5 mA/cm<sup>2</sup> for a CdS cell assuming a 2.4 eV band gap for CdS.<sup>79</sup> In fact, Cu<sub>3-x</sub>P has recently been incorporated into a ZnSnP<sub>2</sub> solar cell<sup>22</sup> but rather as a hole contact than as an absorber.

Finally, one computational study found a small—but nonzero—band gap in pristine Cu<sub>3</sub>P by first-principles calculations using hybrid exchange correlation functionals and a Gaussian-type atomic orbital basis set.<sup>80</sup> A band gap of 0.68 eV was obtained with the PBE0 functional, and a 0.18 eV gap was obtained with the HSE06 functional. However, unusually large values of the on-site Hubbard repulsion (*U*) were necessary to reproduce these band gaps by the DFT+*U* approach<sup>81</sup> using a plane wave basis set. It is also unusual that Hubbard repulsion had to be added on the P 3p orbitals rather than just on the Cu 3d orbitals. Most importantly, the complex dielectric function calculated from the DFT+*U* band structure in the same study<sup>80</sup> is incompatible with our present experimental results. As an example, the constant value of the calculated  $\epsilon_1$  (around 4) up to 4 eV photon energy<sup>80</sup> is in stark contrast with the high dispersion of the experimental  $\epsilon_1$  (Figure 8a) in this spectral region (negative, up to 15, and negative again).

To summarize this section, there is no conclusive evidence in favor of identification of Cu<sub>3-x</sub>P as a semiconductor without invoking quantum confinement effects.

## CONCLUSION

We found strong evidence that reactively sputtered Cu<sub>3-x</sub>P films are natively doped p-type semimetals over a broad composition and process parameter range. Unlike the case of nonreactive sputtering, Cu<sub>3-x</sub>P films could be synthesized at temperatures significantly higher than 200 °C, where a higher density of native acceptors can be stabilized and, therefore, the p-type conductivity can be higher. We achieved room-temperature electrical resistivities down to  $4.6 \times 10^{-5} \Omega \text{ cm}$ , the lowest reported for Cu<sub>3-x</sub>P samples in any form.

In films deposited at temperatures above 370 °C, the single-phase region of Cu<sub>3-x</sub>P is likely not wider than the Cu<sub>2.9</sub>P–Cu<sub>3.0</sub>P composition range. However, we found some indications that polycrystalline Cu<sub>3-x</sub>P films deposited at room temperature may tolerate a higher deviation from stoichiometry on the Cu-rich side ( $x < 0$ ).

The decreasing resistivity with increasing PH<sub>3</sub> partial pressure, and the preference for Cu-deficient compositions, and the unit cell contraction with decreasing resistivity substantiated the hypothesis that Cu vacancies are responsible for p-type conductivity in Cu<sub>3-x</sub>P. P-type conductivity was retained even when Cu/P > 3, indicating that Cu vacancies are more stable than any compensating donor even under Cu-rich conditions. Interestingly, stoichiometric defect-free Cu<sub>3</sub>P is also predicted to be a semimetal by DFT, though with a much lower carrier concentration and a net excess of electrons rather than holes. This “intrinsic” Cu<sub>3</sub>P may be very challenging to synthesize due to the high stability of Cu vacancies under all process conditions.

Despite the very high concentration of native dopants, the high mobility of Cu<sub>3-x</sub>P films at low temperatures (276 cm<sup>2</sup>/V s) at 10 K) points to surprisingly low ionized impurity scattering rates. By studying transport properties as a function of lattice direction, we observed anisotropy in the electrical conductivity of Cu<sub>3-x</sub>P, with higher conductivities achieved along the *ab*-plane. This trend is in quantitative agreement with the expected inverse proportionality between hole effective masses (higher in the *c*-axis direction) and hole mobility.

A NIR absorption feature somewhat similar to the previously identified LSPR peak of Cu<sub>3-x</sub>P nanoparticles was found. Curiously, DFT calculations indicate that the interband transitions of intrinsic bulk Cu<sub>3-x</sub>P also give rise to an absorption peak in that spectral region. In thin-film samples, interband transitions are a more likely explanation for the experimentally observed peak, rather than a plasmonic response. Finally, Fermi level lowering in increasingly doped Cu<sub>3-x</sub>P films gave rise to an optical effect equivalent to the Burstein–Moss shift. From this effect, the carrier concentration can in principle be estimated from a simple optical transmission measurement.

## ASSOCIATED CONTENT

### Supporting Information

The Supporting Information is available free of charge at <https://pubs.acs.org/doi/10.1021/acs.chemmater.2c03283>.

Extended experimental and computational details, additional SEM images, Raman spectra, Seebeck coefficient and dielectric function measurements, extended discussion of secondary phases, Hall effect measurements, carrier concentration, mobility, and defects (PDF)

## AUTHOR INFORMATION

### Corresponding Authors

**Andrea Crovetto** – Materials Science Center, National Renewable Energy Laboratory, Golden, Colorado 80401, United States; Department of Structure and Dynamics of Energy Materials, Helmholtz-Zentrum Berlin für Materialien und Energie GmbH, 14109 Berlin, Germany; National Centre for Nano Fabrication and Characterization (DTU Nanolab), Technical University of Denmark, 2800 Kongens Lyngby, Denmark; [orcid.org/0000-0003-1499-8740](https://orcid.org/0000-0003-1499-8740); Email: [ancro@dtu.dk](mailto:ancro@dtu.dk)

**Andriy Zakutayev** – Materials Science Center, National Renewable Energy Laboratory, Golden, Colorado 80401, United States; [orcid.org/0000-0002-3054-5525](https://orcid.org/0000-0002-3054-5525); Email: [andriy.zakutayev@nrel.gov](mailto:andriy.zakutayev@nrel.gov)

### Author

**Thomas Unold** – Department of Structure and Dynamics of Energy Materials, Helmholtz-Zentrum Berlin für Materialien und Energie GmbH, 14109 Berlin, Germany; [orcid.org/0000-0002-5750-0693](https://orcid.org/0000-0002-5750-0693)

Complete contact information is available at: <https://pubs.acs.org/10.1021/acs.chemmater.2c03283>

### Notes

The authors declare no competing financial interest.

## ACKNOWLEDGMENTS

This project has received funding from the European Union's Horizon 2020 research and innovation programme under the Marie Skłodowska-Curie Grant Agreement No. 840751 (synthesis, characterization, simulation, and data analysis work). This work was authored in part at the National Renewable Energy Laboratory, operated by Alliance for Sustainable Energy, LLC, for the U.S. Department of Energy (DOE) under Contract No. DE-AC36-08GO28308. Funding supporting development and operation of synthesis and characterization equipment was provided by the Office of Science, Office of Basic Energy Sciences. We acknowledge Karen N. Heinselman for evaporation of metal contacts and RBS measurements. A.C. is grateful to Søren Raza, Mark K. Svendsen, and Francesco Ricci for useful feedback on optical properties, DFT calculations, and transport calculations.

## REFERENCES

- (1) Minami, T.; Nishi, Y.; Miyata, T. Efficiency Enhancement Using a  $\text{Zn}_{1-x}\text{Ge}_x\text{O}$  Thin Film as an n-Type Window Layer in  $\text{Cu}_2\text{O}$ -based Heterojunction Solar Cells. *Applied Physics Express* **2016**, *9*, 052301.
- (2) Kazimierzczuk, T.; Fröhlich, D.; Scheel, S.; Stolz, H.; Bayer, M. Giant Rydberg Excitons in the Copper Oxide  $\text{Cu}_2\text{O}$ . *Nature* **2014**, *514*, 343–347.
- (3) Hall, R.; Meakin, J. The Design and Fabrication of High Efficiency Thin Film  $\text{CdS}/\text{Cu}_2\text{S}$  Solar Cells. *Thin Solid Films* **1979**, *63*, 203–211.
- (4) Luther, J. M.; Jain, P. K.; Ewers, T.; Alivisatos, A. P. Localized Surface Plasmon Resonances Arising from Free Carriers in Doped Quantum Dots. *Nat. Mater.* **2011**, *10*, 361–366.
- (5) Liu, H.; Shi, X.; Xu, F.; Zhang, L.; Zhang, W.; Chen, L.; Li, Q.; Uher, C.; Day, T.; Snyder, G. J. Copper Ion Liquid-like Thermoelectrics. *Nat. Mater.* **2012**, *11*, 422–425.
- (6) Zhao, K.; Liu, K.; Yue, Z.; Wang, Y.; Song, Q.; Li, J.; Guan, M.; Xu, Q.; Qiu, P.; Zhu, H.; Chen, L.; Shi, X. Are  $\text{Cu}_2\text{Te}$ -Based Compounds Excellent Thermoelectric Materials? *Adv. Mater.* **2019**, *31*, 1903480.
- (7) Yang, C.; Kneiß, M.; Lorenz, M.; Grundmann, M. Room-Temperature Synthesized Copper Iodide Thin Film as Degenerate p-Type Transparent Conductor with a Boosted Figure of Merit. *Proc. Natl. Acad. Sci. U. S. A.* **2016**, *113*, 12929–12933.
- (8) Crovetto, A.; Hempel, H.; Rusu, M.; Choubrac, L.; Kojda, D.; Habicht, K.; Unold, T. Water Adsorption Enhances Electrical Conductivity in Transparent p-Type  $\text{CuI}$ . *ACS Appl. Mater. Interfaces* **2020**, *12*, 48741–48747.
- (9) Yang, C.; Souchay, D.; Kneiß, M.; Bogner, M.; Wei, H. M.; Lorenz, M.; Oeckler, O.; Benstetter, G.; Fu, Y. Q.; Grundmann, M. Transparent Flexible Thermoelectric Material Based on Non-Toxic Earth-Abundant p-Type Copper Iodide Thin Film. *Nat. Commun.* **2017**, *8*, 16076.
- (10) Zakutayev, A.; Caskey, C. M.; Fioretti, A. N.; Ginley, D. S.; Vidal, J.; Stevanović, V.; Tea, E.; Lany, S. Defect Tolerant Semiconductors for Solar Energy Conversion. *J. Phys. Chem. Lett.* **2014**, *5*, 1117–1125.
- (11) Caskey, C. M.; Richards, R. M.; Ginley, D. S.; Zakutayev, A. Thin Film Synthesis and Properties of Copper Nitride, a Metastable Semiconductor. *Mater. Horiz.* **2014**, *1*, 424–430.
- (12) Crovetto, A.; Kojda, D.; Yi, F.; Heinselman, K. N.; LaVan, D. A.; Habicht, K.; Unold, T.; Zakutayev, A. Crystallize It before It Diffuses: Kinetic Stabilization of Thin-Film Phosphorus-Rich Semiconductor  $\text{CuP}_2$ . *J. Am. Chem. Soc.* **2022**, *144*, 13334–13343.
- (13) Olofsson, O.; Holmlund, L.; Ingri, N.; Tricker, M. J.; Svensson, S. The Crystal Structure of  $\text{Cu}_3\text{P}$ . *Acta Chemica Scandinavica* **1972**, *26*, 2777–2787.
- (14) Robertson, D. S.; Snowball, G.; Webber, H. The Preparation and Properties of Single Crystal Copper Phosphide. *J. Mater. Sci.* **1980**, *15*, 256–258.
- (15) Juza, R.; Bär, K. Leiter Und Halbleiter Unter Den Phosphiden Der Ersten Und Zweiten Nebengruppe. *Zeitschrift für anorganische und allgemeine Chemie* **1956**, *283*, 230–245.
- (16) Ann Aitken, J.; Ganzha-Hazen, V.; Brock, S. L. Solvothermal Syntheses of  $\text{Cu}_3\text{P}$  via Reactions of Amorphous Red Phosphorus with a Variety of Copper Sources. *J. Solid State Chem.* **2005**, *178*, 970–975.
- (17) Wolff, A.; Pallmann, J.; Boucher, R.; Weiz, A.; Brunner, E.; Doert, T.; Ruck, M. Resource-Efficient High-Yield Ionothermal Synthesis of Microcrystalline  $\text{Cu}_{3-x}\text{P}$ . *Inorg. Chem.* **2016**, *55*, 8844–8851.
- (18) Wolff, A.; et al. Low-Temperature Tailoring of Copper-Deficient  $\text{Cu}_{3-x}\text{P}$ —Electric Properties, Phase Transitions, and Performance in Lithium-Ion Batteries. *Chem. Mater.* **2018**, *30*, 7111–7123.
- (19) Fritz, H. P.; Rüger, V. Electrochemical Deposition of Copper Phosphides. *Monatshefte für Chemie Chemical Monthly* **1992**, *123*, 397–403.
- (20) Read, C. G.; Callejas, J. F.; Holder, C. F.; Schaak, R. E. General Strategy for the Synthesis of Transition Metal Phosphide Films for Electrocatalytic Hydrogen and Oxygen Evolution. *ACS Appl. Mater. Interfaces* **2016**, *8*, 12798–12803.
- (21) Pawar, S. M.; Pawar, B. S.; Babar, P. T.; Aqueel Ahmed, A. T.; Chavan, H. S.; Jo, Y.; Cho, S.; Kim, J. H. J.; Inamdar, A. I.; Kim, J. H. J.; Kim, H.; Im, H. Electrosynthesis of Copper Phosphide Thin Films for Efficient Water Oxidation. *Mater. Lett.* **2019**, *241*, 243–247.
- (22) Kuwano, T.; Katsube, R.; Kazumi, K.; Nose, Y. Performance Enhancement of  $\text{ZnSnP}_2$  Solar Cells by a  $\text{Cu}_3\text{P}$  Back Buffer Layer. *Sol. Energy Mater. Sol. Cells* **2021**, *221*, 110891.
- (23) Lee, S. W.; Kim, J. M.; Woo, S.-G.; Park, Y.; Yoon, J. C.; Park, H. J.; Kim, N. Y.; Shin, H. S.; Lee, Z. Epitaxially Grown Copper Phosphide ( $\text{Cu}_3\text{P}$ ) Nanosheets Nanoarchitecture Compared with Film Morphology for Energy Applications. *Surfaces and Interfaces* **2021**, *26*, 101369.
- (24) Manna, G.; Bose, R.; Pradhan, N. Semiconducting and Plasmonic Copper Phosphide Platelets. *Angew. Chem., Int. Ed.* **2013**, *52*, 6762–6766.
- (25) Tian, J.; Liu, Q.; Cheng, N.; Asiri, A. M.; Sun, X. Self-Supported  $\text{Cu}_3\text{P}$  Nanowire Arrays as an Integrated High-Performance Three-Dimensional Cathode for Generating Hydrogen from Water. *Angew. Chem., Int. Ed.* **2014**, *53*, 9577–9581.
- (26) De Trizio, L.; Gaspari, R.; Bertoni, G.; Kriegel, I.; Moretti, L.; Scotognella, F.; Maserati, L.; Zhang, Y.; Messina, G. C.; Prato, M.; Marras, S.; Cavalli, A.; Manna, L.  $\text{Cu}_{3-x}\text{P}$  Nanocrystals as a Material Platform for Near-Infrared Plasmonics and Cation Exchange Reactions. *Chem. Mater.* **2015**, *27*, 1120–1128.
- (27) Hou, C.-C.; Chen, Q.-Q.; Wang, C.-J.; Liang, F.; Lin, Z.; Fu, W.-F.; Chen, Y. Self-Supported Cedarlike Semimetallic  $\text{Cu}_3\text{P}$  Nanoarrays as a 3D High-Performance Janus Electrode for Both Oxygen and Hydrogen Evolution under Basic Conditions. *ACS Appl. Mater. Interfaces* **2016**, *8*, 23037–23048.
- (28) Yue, X.; Yi, S.; Wang, R.; Zhang, Z.; Qiu, S. A Novel and Highly Efficient Earth-Abundant  $\text{Cu}_3\text{P}$  with  $\text{TiO}_2$  “P–N” Heterojunction Nanophotocatalyst for Hydrogen Evolution from Water. *Nanoscale* **2016**, *8*, 17516–17523.
- (29) Mu, H.; Liu, Z.; Bao, X.; Wan, Z.; Liu, G.; Li, X.; Shao, H.; Xing, G.; Shabbir, B.; Li, L.; Sun, T.; Li, S.; Ma, W.; Bao, Q. Highly Stable and Repeatable Femtosecond Soliton Pulse Generation from Saturable Absorbers Based on Two-Dimensional  $\text{Cu}_{3-x}\text{P}$  Nanocrystals. *Frontiers of Optoelectronics* **2020**, *13*, 139–148.
- (30) Fu, Z.; Ma, X.; Xia, B.; Hu, X.; Fan, J.; Liu, E. Efficient Photocatalytic  $\text{H}_2$  Evolution over Cu and  $\text{Cu}_3\text{P}$  Co-Modified  $\text{TiO}_2$  Nanosheet. *Int. J. Hydrogen Energy* **2021**, *46*, 19373–19384.
- (31) Stan, M. C.; Klöpsch, R.; Bhaskar, A.; Li, J.; Passerini, S.; Winter, M.  $\text{Cu}_3\text{P}$  Binary Phosphide: Synthesis via a Wet Mechanochemical Method and Electrochemical Behavior as Negative Electrode Material for Lithium-Ion Batteries. *Adv. Energy Mater.* **2013**, *3*, 231–238.

- (32) Liu, S.; He, X.; Zhu, J.; Xu, L.; Tong, J.  $\text{Cu}_3\text{P}/\text{RGO}$  Nanocomposite as a New Anode for Lithium-Ion Batteries. *Sci. Rep.* **2016**, *6*, 35189.
- (33) Peng, X.; Lv, Y.; Fu, L.; Chen, F.; Su, W.; Li, J.; Zhang, Q.; Zhao, S. Photoluminescence Properties of Cuprous Phosphide Prepared through Phosphating Copper with a Native Oxide Layer. *RSC Adv.* **2021**, *11*, 34095–34100.
- (34) Talley, K. R.; Bauers, S. R.; Melamed, C. L.; Papac, M. C.; Heinselman, K. N.; Khan, I.; Roberts, D. M.; Jacobson, V.; Mis, A.; Brennecke, G. L.; Perkins, J. D.; Zakutayev, A. COMBIgor: Data-Analysis Package for Combinatorial Materials Science. *ACS Comb. Sci.* **2019**, *21*, 537–547.
- (35) Talley, K. R.; White, R.; Wunder, N.; Eash, M.; Schwarting, M.; Evenson, D.; Perkins, J. D.; Tumas, W.; Munch, K.; Phillips, C.; Zakutayev, A. Research Data Infrastructure for High-Throughput Experimental Materials Science. *Patterns* **2021**, *2*, 100373.
- (36) Zakutayev, A.; Wunder, N.; Schwarting, M.; Perkins, J. D.; White, R.; Munch, K.; Tumas, W.; Phillips, C. An Open Experimental Database for Exploring Inorganic Materials. *Scientific Data* **2018**, *5*, 180053.
- (37) Schnepf, R. R.; Crovetto, A.; Gorai, P.; Park, A.; Holtz, M.; Heinselman, K. N.; Bauers, S. R.; Brooks Tellekamp, M.; Zakutayev, A.; Greenaway, A. L.; Toberer, E. S.; Tamboli, A. C. Reactive Phosphine Combinatorial Co-Sputtering of Cation Disordered  $\text{ZnGeP}_2$  Films. *Journal of Materials Chemistry C* **2022**, *10*, 870–879.
- (38) Crovetto, A.; Adamczyk, J. M.; Schnepf, R. R.; Perkins, C. L.; Hempel, H.; Bauers, S. R.; Toberer, E. S.; Tamboli, A. C.; Unold, T.; Zakutayev, A. Boron Phosphide Films by Reactive Sputtering: Searching for a P-Type Transparent Conductor. *Advanced Materials Interfaces* **2022**, *9*, 2200031.
- (39) Willis, J.; Bravić, I.; Schnepf, R. R.; Heinselman, K. N.; Monserrat, B.; Unold, T.; Zakutayev, A.; Scanlon, D. O.; Crovetto, A. Prediction and Realisation of High Mobility and Degenerate P-Type Conduction in  $\text{CaCuP}$  Thin Films. *Chemical Science* **2022**, *13*, 5872–5883.
- (40) Blöchl, P. E. Projector Augmented-Wave Method. *Phys. Rev. B* **1994**, *50*, 17953–17979.
- (41) Mortensen, J.; Hansen, L.; Jacobsen, K. Real-Space Grid Implementation of the Projector Augmented Wave Method. *Phys. Rev. B* **2005**, *71*, 035109.
- (42) Enkovaara, J.; et al. Electronic Structure Calculations with GPAW: A Real-Space Implementation of the Projector Augmented-Wave Method. *J. Phys.: Condens. Matter* **2010**, *22*, 253202.
- (43) Perdew, J. P.; Burke, K.; Ernzerhof, M. Generalized Gradient Approximation Made Simple. *Phys. Rev. Lett.* **1996**, *77*, 3865–3868.
- (44) Gritsenko, O.; van Leeuwen, R.; van Lenthe, E.; Baerends, E. J. Self-Consistent Approximation to the Kohn-Sham Exchange Potential. *Phys. Rev. A* **1995**, *51*, 1944–1954.
- (45) Yan, J.; Mortensen, J. J.; Jacobsen, K. W.; Thygesen, K. S. Linear Density Response Function in the Projector Augmented Wave Method: Applications to Solids, Surfaces, and Interfaces. *Phys. Rev. B* **2011**, *83*, 245122.
- (46) Madsen, G. K.; Carrete, J.; Verstraete, M. J. BoltzTraP2, a Program for Interpolating Band Structures and Calculating Semi-Classical Transport Coefficients. *Comput. Phys. Commun.* **2018**, *231*, 140–145.
- (47) Bruno, G.; Losurdo, M.; Capezzuto, P. Study of the Phosphine Plasma Decomposition and Its Formation by Ablation of Red Phosphorus in Hydrogen Plasma. *Journal of Vacuum Science and Technology A: Vacuum, Surfaces, and Films* **1995**, *13*, 349–358.
- (48) Ruck, M.; Hoppe, D.; Wahl, B.; Simon, P.; Wang, Y.; Seifert, G. Fibrous Red Phosphorus. *Angew. Chem., Int. Ed.* **2005**, *44*, 7616–7619.
- (49) Schlenger, H.; Jacobs, H.; Juza, R. Ternäre Phasen Des Lithiums Mit Kupfer Und Phosphor. *Zeitschrift für anorganische und allgemeine Chemie* **1971**, *385*, 177–201.
- (50) Tsai, H.; et al. High-Efficiency Two-Dimensional Ruddlesden–Popper Perovskite Solar Cells. *Nature* **2016**, *536*, 312–316.
- (51) Crovetto, A.; Hajjifarassar, A.; Hansen, O.; Seger, B.; Chorkendorff, I.; Vesborg, P. C. K. Parallel Evaluation of the  $\text{BiI}_3$ ,  $\text{BiOI}$ , and  $\text{Ag}_3\text{BiI}_6$  Layered Photoabsorbers. *Chem. Mater.* **2020**, *32*, 3385–3395.
- (52) Crovetto, A.; Ottsen, T. S.; Stamate, E.; Kjær, D.; Schou, J.; Hansen, O. On Performance Limitations and Property Correlations of Al-doped ZnO Deposited by Radio-Frequency Sputtering. *J. Phys. D: Appl. Phys.* **2016**, *49*, 295101.
- (53) Kroumova, E.; Aroyo, M.; Perez-Mato, J.; Kirov, A.; Capillas, C.; Ivantchev, S.; Wondratschek, H. Bilbao Crystallographic Server: Useful Databases and Tools for Phase-Transition Studies. *Phase Transitions* **2003**, *76*, 155–170.
- (54) Dingle, R. Scattering of Electrons and Holes by Charged Donors and Acceptors in Semiconductors. *London, Edinburgh, and Dublin Philosophical Magazine and Journal of Science* **1955**, *46*, 831–840.
- (55) Wiley, J. D.; DiDomenico, M. Lattice Mobility of Holes in III-V Compounds. *Phys. Rev. B* **1970**, *2*, 427–433.
- (56) Ellmer, K. In *Handbook of Transparent Conductors*; Ginley, D. S., Ed.; Springer US: Boston, MA, 2011; pp 193–263.
- (57) Ravich, Y. I.; Efimova, B. A.; Tamarchenko, V. I. Scattering of Current Carriers and Transport Phenomena in Lead Chalcogenides II. Experiment. *physica status solidi (b)* **1971**, *43*, 453–469.
- (58) Jain, A.; Ong, S. P.; Hautier, G.; Chen, W.; Richards, W. D.; Dacek, S.; Cholia, S.; Gunter, D.; Skinner, D.; Ceder, G.; Persson, K. A. Commentary: The Materials Project: A Materials Genome Approach to Accelerating Materials Innovation. *APL Materials* **2013**, *1*, 011002.
- (59) Sham, L. J.; Schlüter, M. Density-Functional Theory of the Band Gap. *Phys. Rev. B* **1985**, *32*, 3883–3889.
- (60) Kim, S.; Lee, M.; Hong, C.; Yoon, Y.; An, H.; Lee, D.; Jeong, W.; Yoo, D.; Kang, Y.; Youn, Y.; Han, S. A Band-Gap Database for Semiconducting Inorganic Materials Calculated with Hybrid Functional. *Scientific Data* **2020**, *7*, 387.
- (61) Heyd, J.; Peralta, J. E.; Scuseria, G. E.; Martin, R. L. Energy Band Gaps and Lattice Parameters Evaluated with the Heyd-Scuseria-Ernzerhof Screened Hybrid Functional. *J. Chem. Phys.* **2005**, *123*, 174101.
- (62) Ashcroft, N. W.; Mermin, N. D. *Solid State Physics*; Holt, Rinehart, and Winston: 1976.
- (63) Zhang, Y.; Tan, Y.-W.; Stormer, H. L.; Kim, P. Experimental Observation of the Quantum Hall Effect and Berry's Phase in Graphene. *Nature* **2005**, *438*, 201–204.
- (64) Ricci, F.; Chen, W.; Aydemir, U.; Snyder, G. J.; Rignanese, G.-M.; Jain, A.; Hautier, G. An Ab Initio Electronic Transport Database for Inorganic Materials. *Scientific Data* **2017**, *4*, 170085.
- (65) May, A. F.; Snyder, G. J. In *Thermoelectrics and Its Energy Harvesting*; Rowe, D. M., Ed.; CRC Press: 2012.
- (66) Crovetto, A.; Hansen, O. What Is the Band Alignment of  $\text{Cu}_2\text{ZnSn}(\text{S},\text{Se})_4$  Solar Cells? *Sol. Energy Mater. Sol. Cells* **2017**, *169*, 177–194.
- (67) Postava, K.; Sueki, H.; Aoyama, M.; Yamaguchi, T.; Murakami, K.; Igasaki, Y. Doping Effects on Optical Properties of Epitaxial ZnO Layers Determined by Spectroscopic Ellipsometry. *Appl. Surf. Sci.* **2001**, *175–176*, 543–548.
- (68) Bertoni, G.; Ramasse, Q.; Brescia, R.; De Trizio, L.; De Donato, F.; Manna, L. Direct Quantification of Cu Vacancies and Spatial Localization of Surface Plasmon Resonances in Copper Phosphide Nanocrystals. *ACS Materials Letters* **2019**, *1*, 665–670.
- (69) Jasperson, S. N.; Schnatterly, S. E. Photon-Surface-Plasmon Coupling in Thick Ag Foils. *Phys. Rev.* **1969**, *188*, 759–770.
- (70) Kaspar, W.; Kreibitz, U. Surface Structure Influences on the Absorptance of Thick Silver Films. *Surf. Sci.* **1977**, *69*, 619–636.
- (71) Burstein, E. Anomalous Optical Absorption Limit in InSb. *Phys. Rev.* **1954**, *93*, 632–633.
- (72) Sernelius, B. E.; Berggren, K.-F.; Jin, Z.-C.; Hamberg, I.; Granqvist, C. G. Band-Gap Tailoring of ZnO by Means of Heavy Al Doping. *Phys. Rev. B* **1988**, *37*, 10244–10248.

(73) Momma, K.; Izumi, F. VESTA 3 for Three-Dimensional Visualization of Crystal, Volumetric and Morphology Data. *J. Appl. Crystallogr.* **2011**, *44*, 1272–1276.

(74) Perdew, J. P.; Ruzsinszky, A.; Csonka, G. I.; Vydrov, O. A.; Scuseria, G. E.; Constantin, L. A.; Zhou, X.; Burke, K. Restoring the Density-Gradient Expansion for Exchange in Solids and Surfaces. *Phys. Rev. Lett.* **2008**, *100*, 136406.

(75) Weber, A.; Sutter, P.; von Känel, H. Optical, Electrical, and Photoelectrical Properties of Sputtered Thin Amorphous Zn<sub>3</sub>P<sub>2</sub> Films. *J. Appl. Phys.* **1994**, *75*, 7448–7455.

(76) Zawadzki, P.; Zakutayev, A.; Lany, S. Entropy-Driven Clustering in Tetrahedrally Bonded Multinary Materials. *Physical Review Applied* **2015**, *3*, 034007.

(77) Fang, C. M.; de Groot, R. A.; Haas, C. Bulk and Surface Electronic Structure of 1T-TiS<sub>2</sub> and 1T-TiSe<sub>2</sub>. *Phys. Rev. B* **1997**, *56*, 4455–4463.

(78) Shockley, W.; Queisser, H. J. Detailed Balance Limit of Efficiency of P-n Junction Solar Cells. *J. Appl. Phys.* **1961**, *32*, 510.

(79) Crovetto, A.; Cazzaniga, A.; Ettliger, R. B.; Schou, J.; Hansen, O. Large Process-Dependent Variations in Band Alignment and Interface Band Gaps of Cu<sub>2</sub>ZnSnS<sub>4</sub>/CdS Solar Cells. *Sol. Energy Mater. Sol. Cells* **2018**, *187*, 233–240.

(80) Gaspari, R.; Labat, F.; Manna, L.; Adamo, C.; Cavalli, A. Semiconducting and Optical Properties of Selected Binary Compounds by Linear Response DFT+U and Hybrid Functional Methods. *Theor. Chem. Acc.* **2016**, *135*, 73.

(81) Anisimov, V. I.; Zaanen, J.; Andersen, O. K. Band Theory and Mott Insulators: Hubbard U Instead of Stoner I. *Phys. Rev. B* **1991**, *44*, 943–954.

## Recommended by ACS

### Formation and Transformation of Cu<sub>2-x</sub>Se<sub>1-y</sub>Te<sub>y</sub> Nanoparticles Synthesized by Tellurium Anion Exchange of Copper Selenide

Katherine L. Thompson, Raymond E. Schaak, *et al.*

MARCH 07, 2023  
INORGANIC CHEMISTRY

READ 

### Revealing Hidden Patterns through Chemical Intuition and Interpretable Machine Learning: A Case Study of Binary Rare-Earth Intermetallics RX

Volodymyr Gvozdzetskyi, Arthur Mar, *et al.*

JANUARY 30, 2023  
CHEMISTRY OF MATERIALS

READ 

### One-Pot Size-Controlled Synthesis of Tin- and Antimony-Based Intermetallic Nanoparticles

Andrew J. McGrath, Sergei A. Ivanov, *et al.*

DECEMBER 27, 2022  
CHEMISTRY OF MATERIALS

READ 

### Nickel Boride (Ni<sub>3</sub>B) Nanocrystals: From Solid-State Synthesis to Highly Colloidally Stable Inks

Jennifer Hong, Loredana Protesescu, *et al.*

FEBRUARY 10, 2023  
CHEMISTRY OF MATERIALS

READ 

Get More Suggestions >